RL-TR-97-194
Final Technical Report
October 1997

BRANCHED-PHOTOCYCLE THREE-DIMENSIONAL MEMORY

Syracuse University

Robert R. Birge

APPROVED FOR PUBLIC RELEASE; DISTRIBUTION UNLIMITED.

Rome Laboratory
Air Force Materiel Command
Rome, New York

This report has been reviewed by the Rome Laboratory Public Affairs Office (PA) and is releasable to the National Technical Information Service (NTIS). At NTIS it will be releasable to the general public, including foreign nations.

RL-TR-97-194 has been reviewed and is approved for publication.

APPROVED: Bernard J Clarke

BERNARD J. CLARKE
Project Engineer

FOR THE DIRECTOR:

JOSEPH CAMERA
Technical Director
Intelligence & Reconnaissance Directorate

If your address has changed or if you wish to be removed from the Rome Laboratory mailing list, or if the addressee is no longer employed by your organization, please notify RL/IRAP, 32 Hangar Road, Rome, NY 13441-4114. This will assist us in maintaining a current mailing list.

Do not return copies of this report unless contractual obligations or notices on a specific document require that it be returned.

REPORT DOCUMENTATION PAGE	Form Approved OMB No. 0704-0188

1. AGENCY USE ONLY *(Leave blank)*	2. REPORT DATE	3. REPORT TYPE AND DATES COVERED
	October 1997	Final Nov 95 - Jun 97

4. TITLE AND SUBTITLE

BRANCHED-PHOTOCYCLE THREE-DIMENSIONAL MEMORY

5. FUNDING NUMBERS

C - F30602-95-C-0135
PE - 62702F
PR - 4594
TA - 15
WU - M4

6. AUTHOR(S)

Robert Birge

7. PERFORMING ORGANIZATION NAME(S) AND ADDRESS(ES)

Syracuse University
W. M. Keck Center for Molecular Electronics
Syracuse, NY 13244-4100

8. PERFORMING ORGANIZATION REPORT NUMBER

N/A

9. SPONSORING/MONITORING AGENCY NAME(S) AND ADDRESS(ES)

Rome Laboratory/IRAP
32 Hangar Road
Rome, NY 13441-4114

10. SPONSORING/MONITORING AGENCY REPORT NUMBER

RL-TR-97-194

11. SUPPLEMENTARY NOTES

Rome Laboratory Project Engineer: Bernard J. Clarke/IRAP/(315) 330-2106

12a. DISTRIBUTION AVAILABILITY STATEMENT

Approved for public release; distribution unlimited.

12b. DISTRIBUTION CODE

13. ABSTRACT *(Maximum 200 words)*

The promise of new architecture and more cost-effective miniaturization has prompted interest in molecular electronics and molecular based optical memories. Nature has already optimized through serendipitous natural selection some molecules for such applications. This effort examines the use of the protein bacteriorhodopsin in a branched-photocycle three-dimensional memory. By using a sequential one-photon process, parallel read and write process can be carried out without disturbing the data outside of the irradiated volume. This final report presents the status, the research and development effort, and an overview of what can be expected in the near future in this area of research.

14. SUBJECT TERMS

Bacteriorhodopsin, Optical Memory, Optical Memory Media

15. NUMBER OF PAGES

44

16. PRICE CODE

17. SECURITY CLASSIFICATION OF REPORT	18. SECURITY CLASSIFICATION OF THIS PAGE	19. SECURITY CLASSIFICATION OF ABSTRACT	20. LIMITATION OF ABSTRACT
UNCLASSIFIED	UNCLASSIFIED	UNCLASSIFIED	UL

Standard Form 298 (Rev. 2-89) (EG)
Prescribed by ANSI Std. 239.18
Designed using Perform Pro, WHS/DIOR, Oct 94

Table of Contents

List of Figures *(Captions are Abbreviated)*

1. Abstract.

The promise of new architectures and more cost-effective miniaturization has prompted interest in molecular electronics and molecular-based optical memories. Nature has already optimized through serendipitous natural selection some molecules for such applications. We examine here the use of the protein bacteriorhodopsin in a branched-photocycle three-dimensional memory. By using a sequential one-photon process, parallel read and write processes can be carried out without disturbing data outside of the irradiated volume. This final report presents the status of our research and development effort and an overview of what can be realistically expected during the next year of work on this project.

The goals of this contract were to fabricate a prototype protein-based volumetric memory based on the branched-photocycle architecture, test the reliability of the memory and optimize the protein-based memory medium. A prototype bench-scale prototype was developed and tested to investigate the viability of the branched-photocycle architecture based on bacteriorhodopsin. The main difference in the present study relative to previous prototype studies was the use of commercially available laser diodes to do both the paging and writing operations. We also replaced the active matrix liquid crystal spatial light modulators with film, because all the commercial modulators produced diffraction and artifacts. A CCD array detector was used to monitor the paged data. A variety of data cuvettes were prepared to test various optical geometries and protein environments. The protein was optimized by using both thermal and chemical modifications, resulting in a five-fold improvement in data write efficiency. Reliability problems remain, but reliability has been improved by a factor of four relative to the earlier Level I prototype. The probability of a read error is now 0.009/bit for symmetric (highly random) data and 0.011/bit for unsymmetric (non-random) data. This error rate must be improved significantly before this memory architecture can be considered to have commercial potential.

2. Rationale and Overview

Bacteriorhodopsin is the light-transducing protein in the purple membrane of *Halobacterium salinarium*, an archaebacterium that inhabits salt marshes [1-5]. This bacterium has survived five mass extinctions during a 3.5 billion year evolutionary period, and has evolved a protein with high photochemical efficiency, photochromic cyclicity and thermal stability [6-12]. A ribbon structure of the protein is shown in Fig. 1. In the native organism, the protein converts light into a proton gradient that is used by the bacterium as a chemiosmotic source of energy.

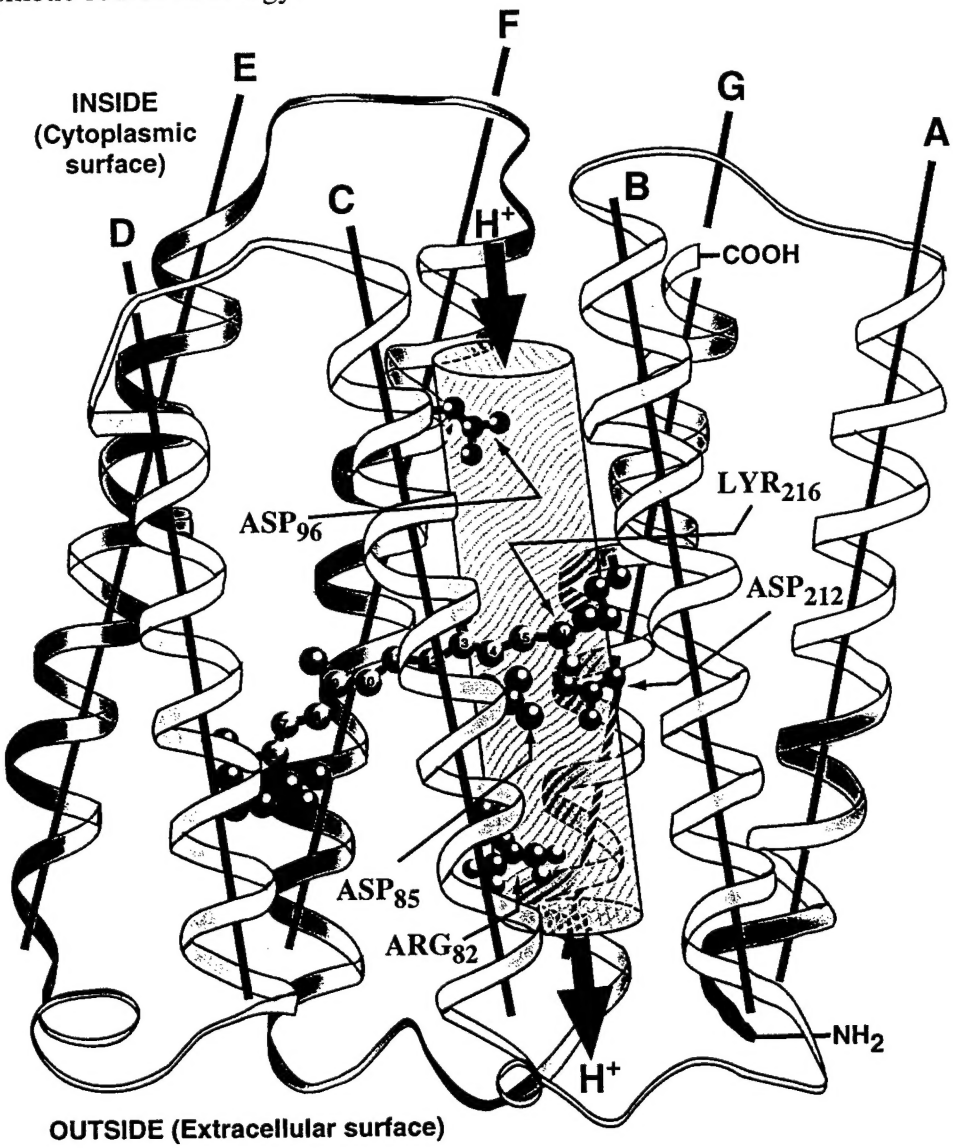

Figure 1. The structure of bacteriorhodopsin is shown using ribbons to represent the seven alpha helical segments that span the membrane. Selected amino acid residues that participate in the proton pumping process are indicated. The shaded gray cylinder (volume $\approx$ 500 Å^3) has a length of about 26 Å and a diameter of about 5 Å and delineates the approximate volumetric region of the proton channel.

Advances in central processor technology have altered the character of computer technology from processor-limited towards memory-limited performance [9]. The overall throughput of many scientific and image analysis problems is now determined primarily by the size and data transfer bandwidths of the random access memory rather than the speed of the central processor unit or the floating point hardware. This situation has generated an increased awareness that new memory architectures providing more cost effective storage capacities, local processing capabilities or data bandwidths should be investigated [13]. Three-dimensional memories store information in a volumetric memory medium and offer as much as a one-thousand fold improvement in data storage capacity for a given enclosure size, although optical and reliability considerations tend to reduce the comparative advantage factor to values closer to 300 [10,11,14,15]. The two most common architectures are based on two-photon [10,13-16] or holographic [17-19] methods. The branched-photocycle architecture explored here is useful because it rigorously excludes photochemistry outside of the doubly irradiated volume, a problem which must be solved before high density volumetric memories can reach their full potential.

The branched-photocycle architecture investigated here was developed in response to problems with the two-photon based architecture. First, high laser intensities are required, which prevent the use of inexpensive laser diodes to write data. This observation is true even though bacteriorhodopsin has one of the largest two-photon absorptivities reported for a broad-band photochromic material [20-22]. Second, unwanted photochemistry invariably occurs along the laser axes, which requires rather complex photochemical cleaning operations to be carried out following the write process [9,23,24]. Third, no protein state which provides for extended lifetime data storage could be created via a direct two-photon process [5]. These three issues suggest that commercialization will not be viable without considerable additional research and development. Fortunately, during the course of these studies we identified a branching reaction of the protein which offers a novel approach to reading and writing data within a three-dimensional polymer cuvette containing the protein.

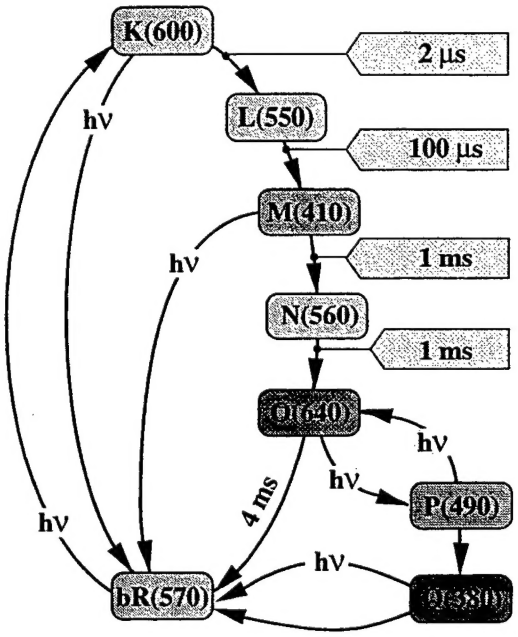

Figure 2. The photocycle of bacteriorhodopsin.

The photocycle of bacteriorhodopsin at 30°C is shown in Fig. 2. The main photocycle is shown in the left-hand portion of the figure and is activated by the primary photochemical event, which converts the resting state, **bR**, into the primary photoproduct, called **K**. The remainder of the photocycle involved thermal reactions which result in reformation of the resting state, **bR**, in about 6-10 milliseconds, depending upon temperature. The last intermediate in the photocycle is called **O**, and this state can be converted by light to form **P**, which subsequently decays to form **Q**. The latter two intermediates are the sole participants in the branching photocycle, which exists as an independent entity from the main photocycle. The key observation here is that this

branching sequence can only be created by a sequential one-photon process. Furthermore, the **Q** state has a lifetime at room temperature of about five years.

Before we discuss the details of the branched-photocycle architecture, it is useful to compare the performance of this architecture relative to the two-photon architecture based on the use of the same protein. A comparison of the sequential one-photon (branched-photocycle) architecture with the simultaneous two-photon architecture based on bacteriorhodopsin is shown in Table I. We note that a majority of the table entries are based on simulations, and thus we must delay final judgment until all the prototyping work is completed. We note, however, that all of the data collected to date indicate that our simulations were either correct or conservative.

Table I. Sequential One-Photon versus Simultaneous Two-Photon Volumetric Memory Architectures Based on Bacteriorhodopsin[a]

Architecture or Property	Two-Photon	One-Photon
Write method	simultaneous 2P	sequential 1P
Molecular representation of zero bit[b]	bR	bR
Molecular representation of one bit[b]	M	P,Q
Parallel write capability	**power/ΔT limited**	*diffraction limited*
Maximum write speed (1024×1024 pixel; per cube)	**~1 MByte/s**	*~10 MByte/s*
Read method	2P photovoltaic	1P paged ΔA
Parallel read capability	***power/ΔT limited***	*diffraction limited*
Maximum read speed (1024×1024 pixel; per cube)	**~1 MByte/s**	*~10 MByte/s*
Bit size in cubic microns (1.6 cm×1.6 cm×2 cm cube)	*~200 μm³*	**~500 μm³**
Storage capacity per cube (1.6 cm×1.6 cm×2 cm)	*~2.3 GByte*	**~1 GByte**
Conversions per photon	**~0.0000001**	*~0.0001*
Unwanted axial photochemistry	***5% - 25%***	*none*
Unwanted axial photochemistry after cleaning	***~2%***	*n/a*
Power required	**~ 1 mJ**	*~0.01 mJ*
Lasers required	**pulsed**	*cw or laser diode*
Signal-to-noise ratio	***1.1***	*1.9*
Temperature for >two year storage	***-10°C***	*10 - 40°C*
Optimal operating temperature	***-10°C***	*30°C*
Shelf life of data at ambient temperature	***weeks–months***	*years*

(a) romant performance neutral; *italics † acceptable or better;*
bold = acceptable but places significant limits on performance;
bold italics = will prevent commercialization unless improved.

(b) In most implementations, both the zero bit and the one bit are represented as linear combinations of **bR** and a second intermediate (**M** in the two-photon memory, and **P:Q** in the sequential one-photon memory). For example, the branched-photocycle memory operates with maximal efficiency by assigning **zero** to [95% **bR** + 5% **P+Q**] and **one** to [85% **bR** + 15% **P+Q**].

3. The Branched–Photocycle Architecture

A basic requirement for the implementation of all branched photocycle volumetric memories is the availability of a molecule or light-transducing protein which undergoes a photocycle upon light activation and which has one or more thermal intermediates within the photocycle which can be photochemically converted into a stable species. Orthogonal light beams are used to activate the branched photocycle only at that location within the volumetric memory cell where the two beams cross and the timing between the light beams is appropriate. We anticipate that the branched-photocycle volumetric architecture can be implemented by using a variety of different molecules and light-transducing proteins. As we demonstrate below, however, bacteriorhodopsin has native properties near-optimal for this implementation. Data can be written, read and stored by using the following optical scheme to access the branched intermediates, **P** and **Q**.

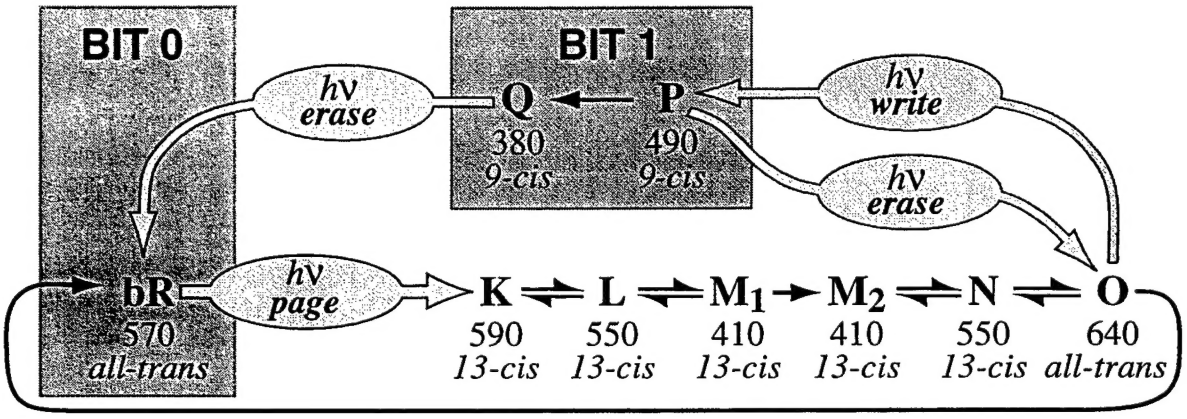

scheme 1

A. Bacteriorhodopsin as an optical AND gate.

Bacteriorhodopsin (MW ≅ 26,000) is the light harvesting protein in the purple membrane of a micro-organism formally known as *Halobacterium salinarium* and commonly called *Halobacterium halobium* [5,8]. The bacterium grows in salt marshes where the concentration of salt is roughly six times higher than that found in sea water. The purple membrane is grown by the bacterium when the concentration of oxygen becomes too low to sustain respiration. The protein, upon the absorption of light, pumps a proton across the membrane generating a chemical and osmotic potential that serves as an alternative source of energy. The fact that the protein must survive in the harsh environment of a salt marsh, where the temperatures can exceed 65°C for extended periods of time, requires a robust protein that is resistant to thermal and photochemical damage. Recent experiments indicate that the protein can withstand temperatures as high as 140°C [7], but under most conditions, denaturation occurs at 80°C. The cyclicity of the protein (i.e. the number of times it can be photochemical cycled) exceeds 10^6 [5,8], a value considerably higher than most synthetic photochromic materials.

The light absorbing chromophore of bacteriorhodopsin is all-trans retinal (vitamin A aldehyde). The chromophore is bound to the protein via a protonated linkage to a lysine residue attached to the protein backbone. The protein bound chromophore carries a positive charge, which interacts elecrostatically with charged amino acids in the protein

binding site. These interactions impart photochemical properties to the chromophore that differ significantly from those observed in the chromophore when in solution. Upon the absorption of light, a rotation around the C_{13}=C_{14} double bond occurs to generate a 13-cis geometry. This process is called a photoisomerization, and in bacteriorhodopsin it is complete in less than one picosecond. The reason for this unusual speed is due to a barrierless excited state potential surface [5]. In this regard, bacteriorhodopsin is a photochemical analog of a high electron mobility transistor (HEMT) device [9].

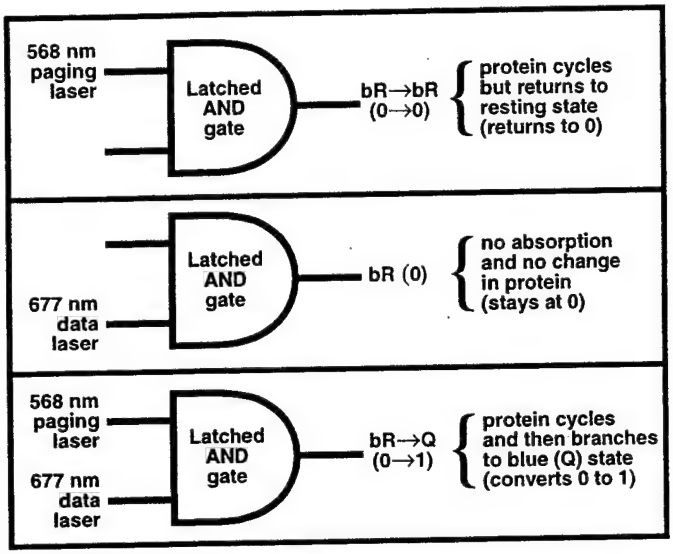

If we assign the **P** and **Q** states as the logical state one, **scheme 1** illustrates the use of the protein as an optically addressed latched AND gate. In other words, the only way to generate a logical one (or in this case, to set bit 1) is to provide two inputs (two photons) at the correct wavelength and timing (see insert at right). This is the key to the rigorous exclusion of unwanted photochemistry and is responsible in part for making the branched-photocycle architecture so attractive in terms of reliability. The quantum efficiency of the primary photochemical event associated with the page selection process is quite high (0.65). This is important in terms of activating an entire page efficiently. The quantum efficiency of the data write process is much lower (0.001 – 0.02), which has both advantages and disadvantages. The advantage is that multiple read operations can be carried out without disturbing the data. The disadvantage is that longer irradiation times (1-4 ms) are required to generate adequate photochemical conversion. The latter problem, however, is circumvented by carrying out as many as 10^6 write operations simultaneously (see below). Note that the two photons are not absorbed simultaneously, and thus this memory operates by a sequential one-photon process, not a simultaneous two-photon process. By activating a page (via the "page" photon) and writing the data (via the "write" photon) by using orthogonal light beams, data can be accessed in three dimensions. The details of these processes are provided in Section 4.

Relatively little is known about the characteristics of the **P** and **Q** states that combine to represent binary state 1. A recent study by Popp et al. provides evidence to indicate that these two states have a 9-cis conformation [12]. Our molecular models of the key states are shown in Fig. 3. By using the same polymer matrix methods as described in our two-photon patent [25], volumetric memory media can be prepared with optimal properties. The details of our current memory media are provided in Section 4.D below.

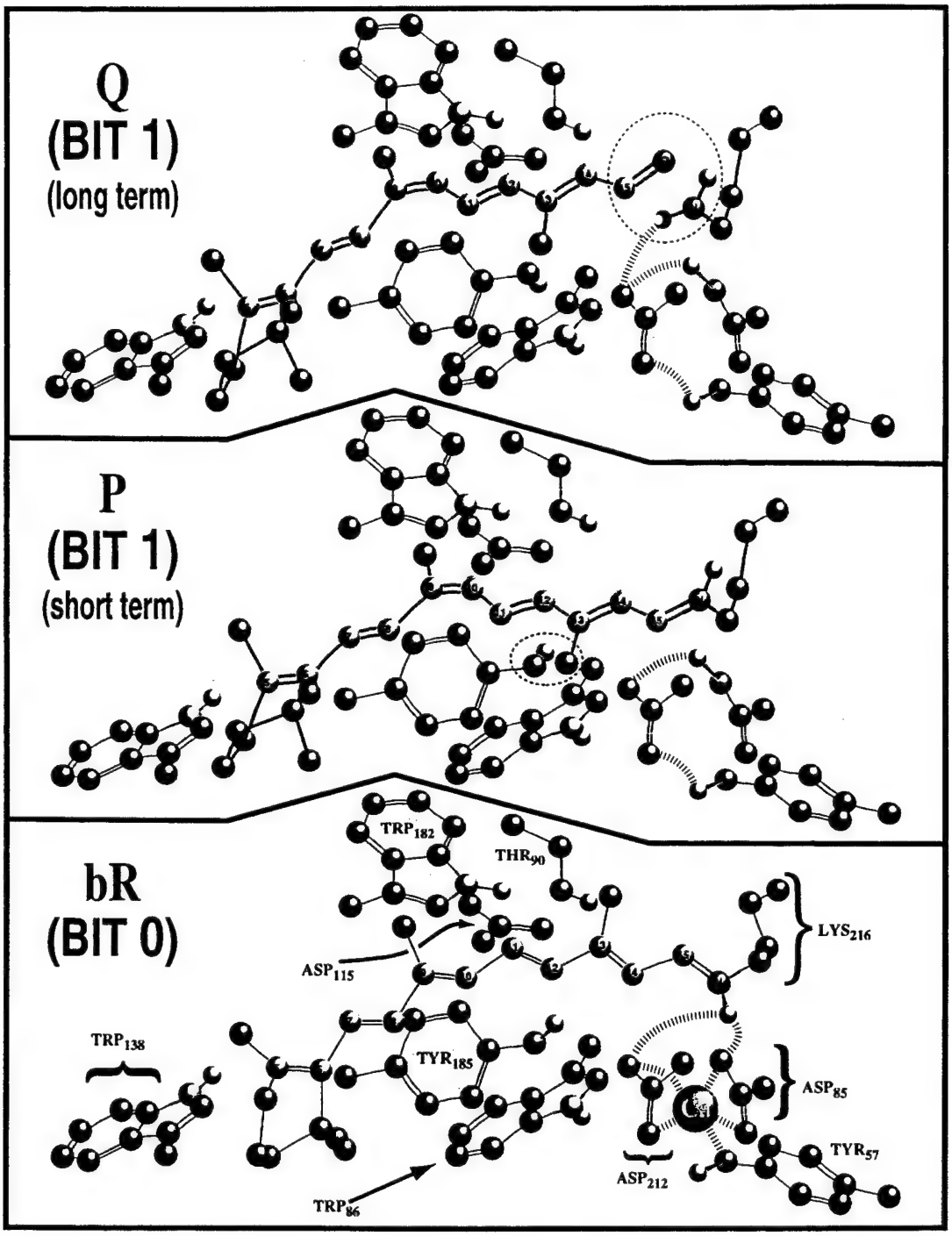

Figure 3. Molecular models of the binding site of bacteriorhodopsin in the resting state (**bR** or BIT 0), the **P** state (short-term BIT 1) and the **Q** state (long-term BIT 1). The location of the calcium ion in **bR** is based on two-photon spectroscopy [22]. The locations of the calcium ion in **P** and **Q** are not known. The chromophore is *all-trans* in **bR** and *9-cis* in **P** and **Q**. The remarkable longevity of the **Q** state is due to the fact that the link to the protein is broken, coupled with the fact that the chromophore remains trapped in the binding site. The only quick way of returning the **Q** state to **bR** is to irradiate it with blue light, which isomerizes *9-cis* back to *all-trans*. This photoisomerization is followed by spontaneous reformation of the chromophore-protein link and regeneration of **bR**.

4. Implementation of the Prototype

In this section we describe the design and fabrication of a bench-scale (Type I) prototype and the methods that are used to write, read and erase data. The key modifications in our prototype relative to our previous studies involves the replacement of the krypton-ion lasers with commercially available diode lasers. A schematic diagram of the prototype is shown in Figures. 4A and 4B. The write and read optical protocols are summarized in Fig. 5 and the absorption spectra of the key intermediates in the main and the branched photocycle are shown in fig. 6.

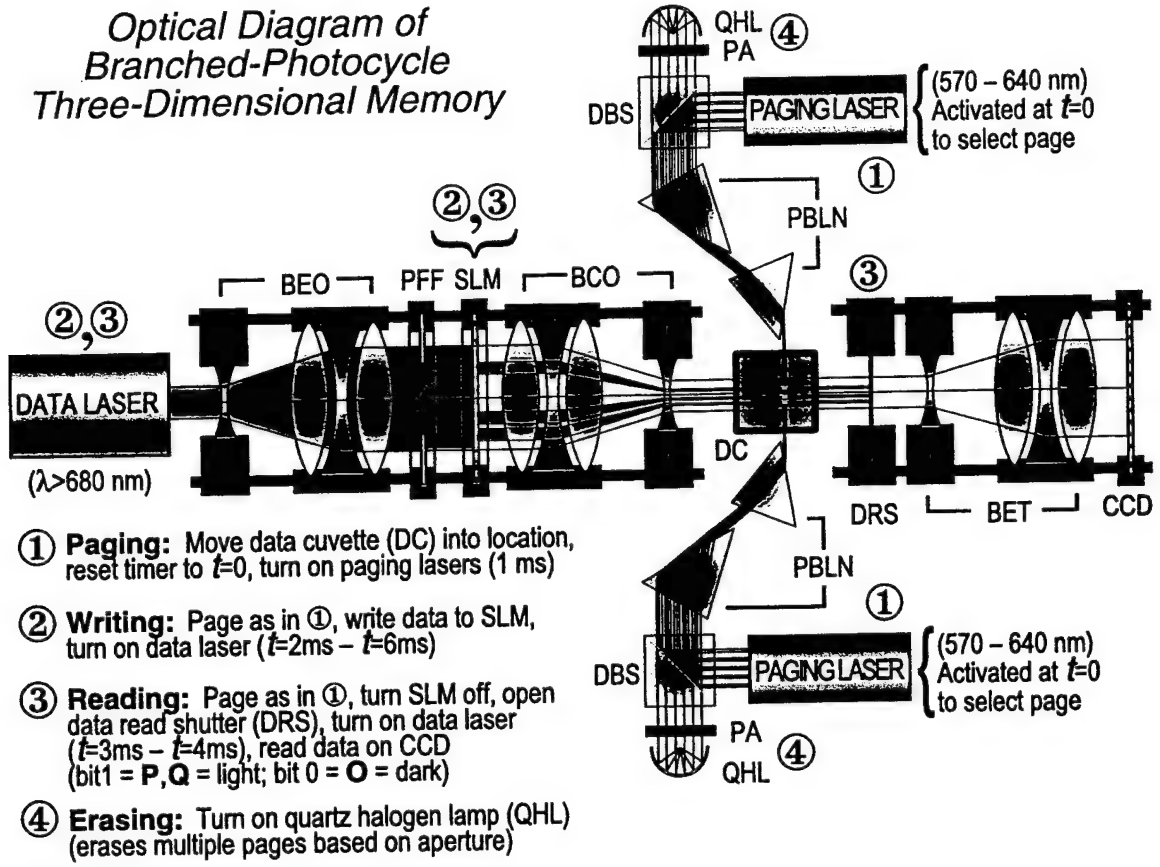

Figure 4A. Optical diagram of the protein-based branched-photocycle optical memory. QHL, quartz halogen lamp (used for data erase); PA, page aperture; DBS, dichroic beam splitter; BEO, beam expanding optics; SLM, spatial light modulator (selects which data bits within the page will be written); BCO, beam condensing optics; DC, data cuvette containing the protein in a transparent polymer matrix; CCD, charge coupled device (reads data); DCKH, data cuvette kinematic holder; PTC, Peltier temperature controller.

Figure 4B (next page): Schematic diagram of the branched-photocycle three-dimensional memory. The four operations associated with the process of data storage, retrieval and erasure are shown. The paging operation precedes both the writing and reading processes; erasure is independent. There are dual paging laser systems (Fig. 2), but we show only one for clarity. The use of incandescent erasure leads to multiple pages being erased simultaneously (see discussion below).

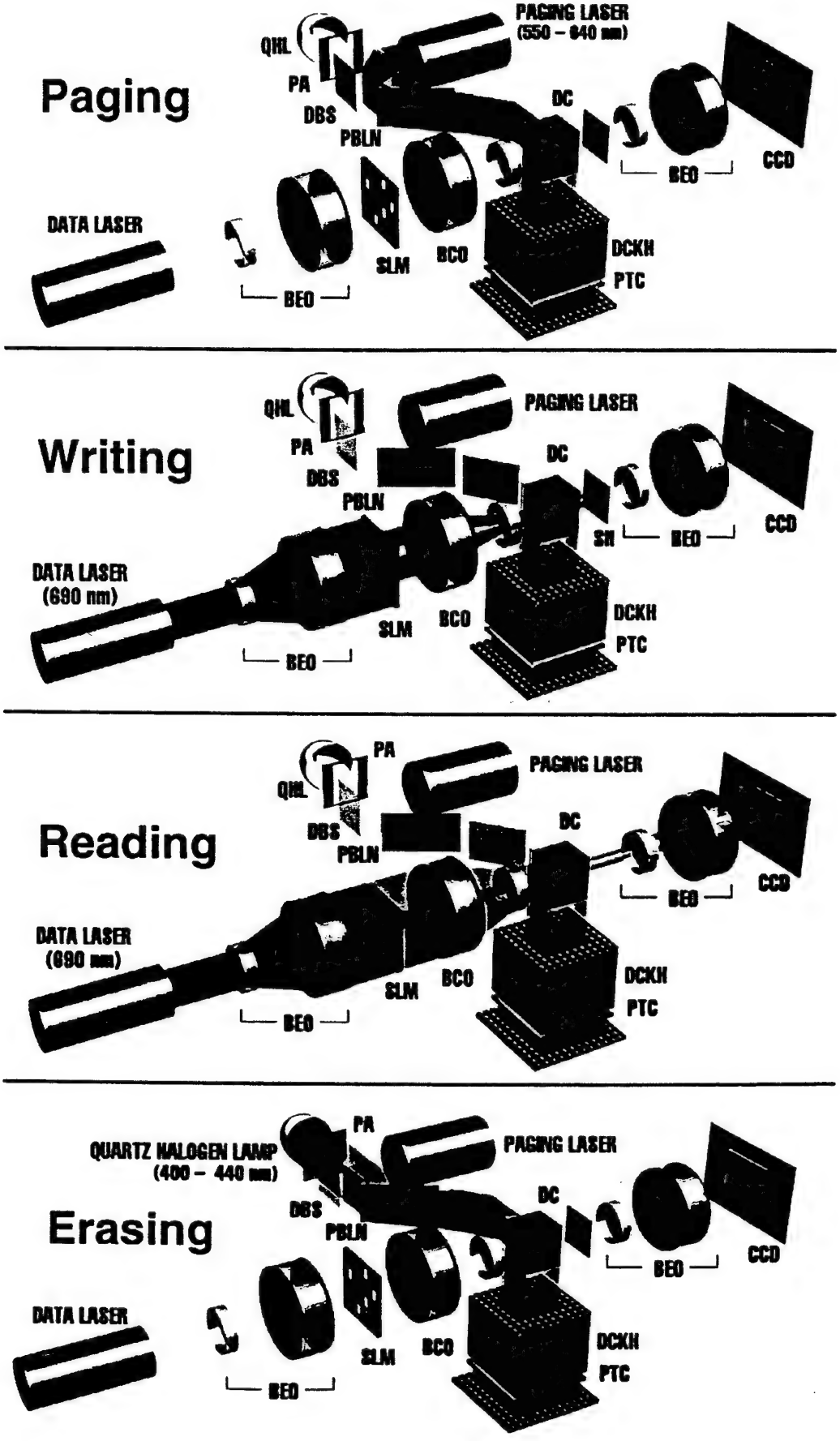

Figure 4B (Caption on previous page)

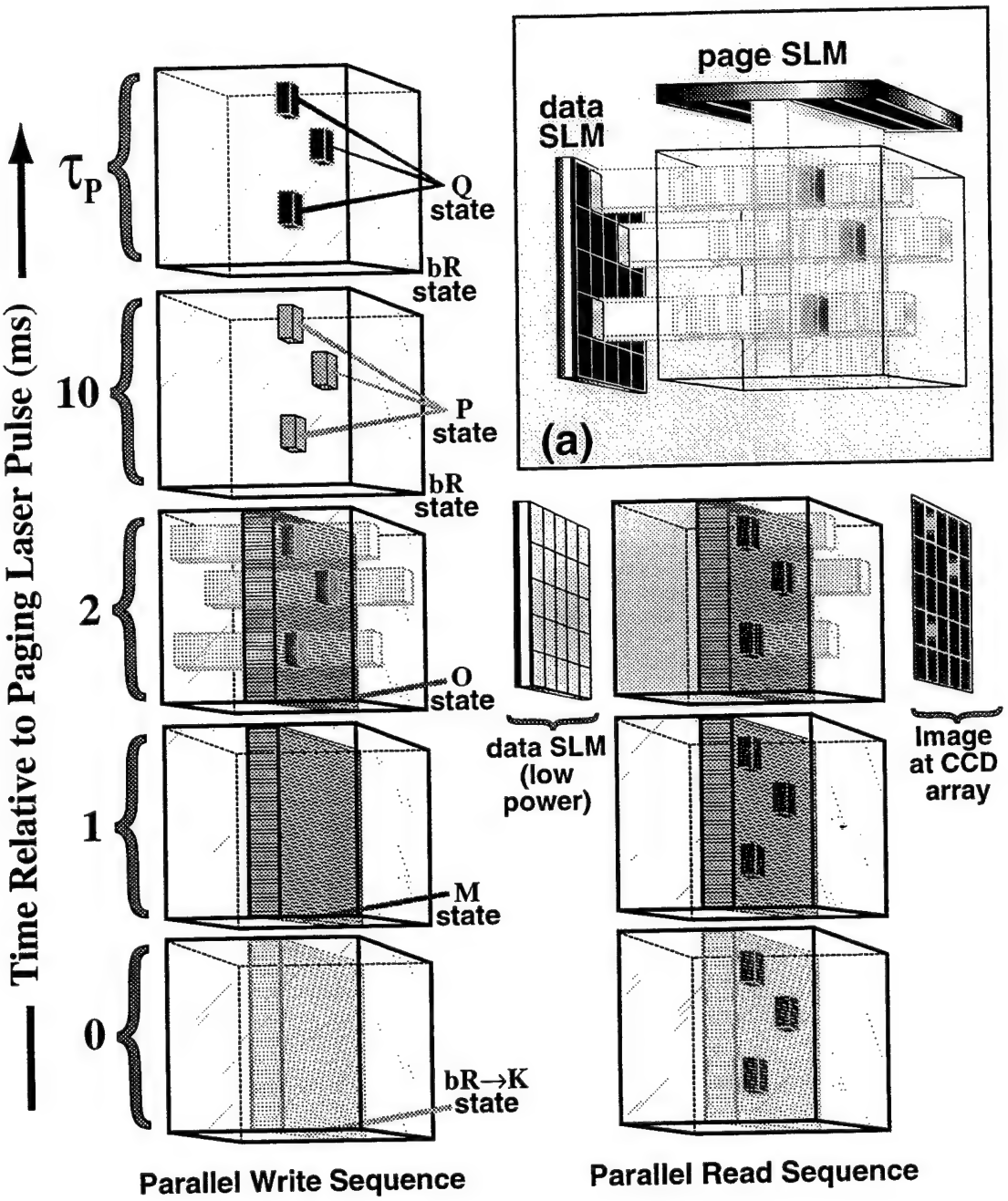

Figure 5. A schematic diagram of the parallel write and read sequences with time progressing from bottom to top. The write sequence (left column) is as follows: (1) turn on the page beam to activate **bR** photocycle, (2) after ~2 ms, activate appropriate 690nm data beams to convert **O** to **P**. The read sequence (right column) is as follows: (1) turn on 568nm page laser to activate **bR** photocycle within paged region only, (2) after ~2 ms, read entire page as an image on the CCD array detector. The basic optical architecture is shown in insert (a).

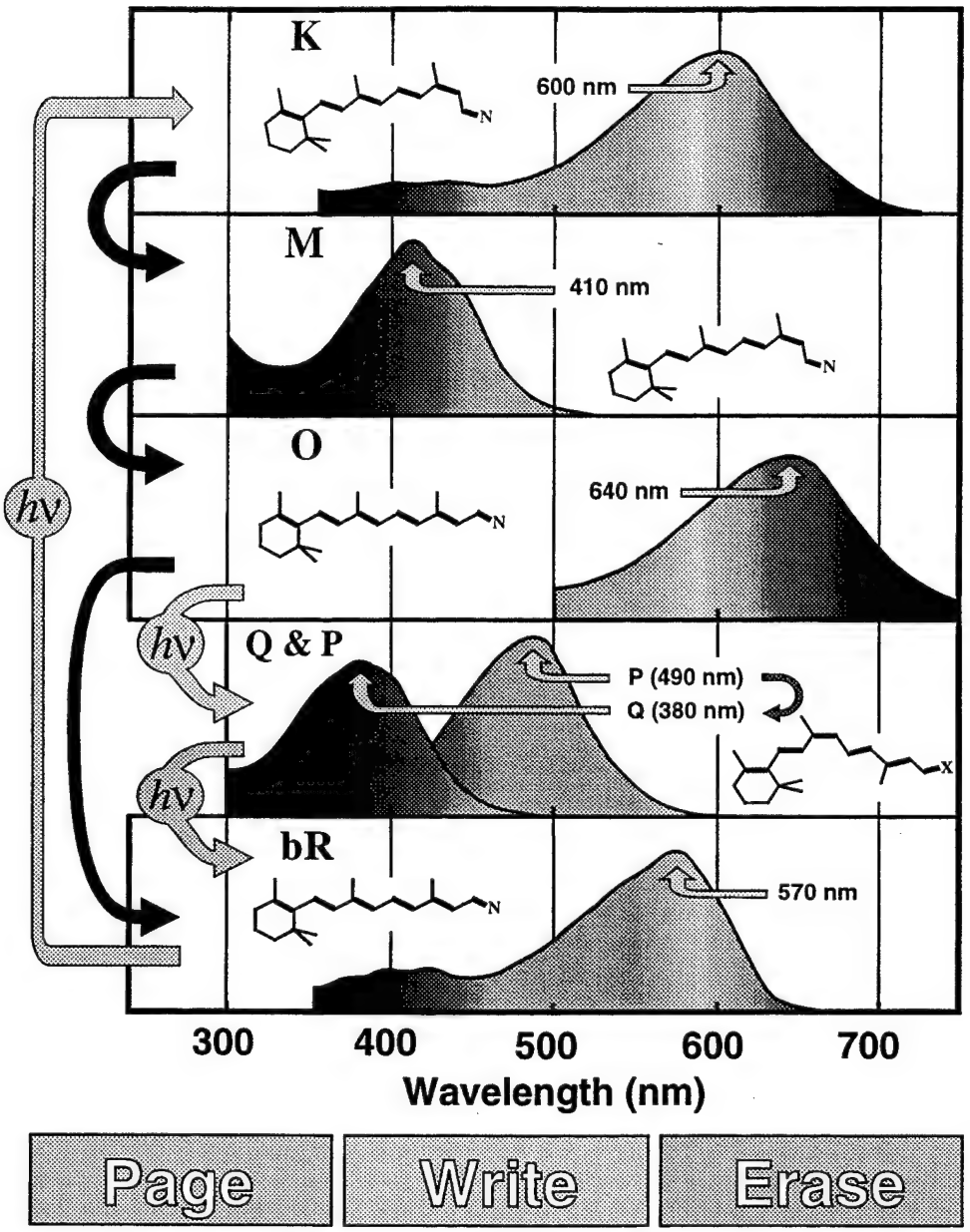

Figure 6. Absorption spectra of selected intermediates in the photocycle of bacteriorhodopsin. Gray arrows indicate light activated processes and black arrows indicate thermal reactions. The structures of the polyene chromophore are shown as inserts [*N* represents nitrogen; *X* represents either nitrogen (in **P**) or oxygen (in **Q**)].

A. Data are written in parallel via a branching reaction.

A parallel write is accomplished by using the sequential one-photon optical protocol shown in Fig. 5. The vertical axis of Fig. 5 charts nominal time relative to the firing of the page addressing (or *paging*) laser. The paging beam ($\lambda = 630$nm, $\Delta t < 1$ ms) activates the photocycle of bacteriorhodopsin and after a few milliseconds the **O** intermediate approaches

maximal concentration. The data laser and the SLM are now activated (λ = 690 nm, $\Delta t \approx$ 3 ms) to irradiate those volume elements into which 1 bits are to be written. This process converts **O** to **P** in these, and only these, locations within the memory cuvette. After many minutes the **P** state thermally decays to form the **Q** state (the $\mathbf{P} \rightarrow \mathbf{Q}$ decay time, τ_P, is highly dependent upon temperature and polymer matrix). The write process is accomplished in ~10 ms, the time it takes the protein to complete the photocycle. This represents an overall write data throughput of ten million characters per second (10 MB/s) for a 1024×1024 data array and two error correcting bits per byte.

B. Data are read in parallel by using differential absorptivity.

The read process takes advantage of the fact that light around 690 nm is absorbed by only two intermediates in the photocycle of light-adapted bacteriorhodopsin, the primary photoproduct **K** and the relatively long-lived **O** intermediate (see Fig 6). A parallel read is accomplished by using a differential absorption process as shown in the right column of Fig. 5. The read sequence starts out in a fashion identical to that of the write process by activating the 568nm paging beam. After two milliseconds, data laser is activated and the data read (DRS) shutter is opened for 1ms, but the SLM is left off allowing only 0.1% of the total laser power through. A CCD array (clocked to clear all charges prior to opening DTS and DRS) images the light passing through the data cuvette. Those elements in binary state 1 (**P** or **Q**) do not absorb the 690nm light, but those volumetric elements that started out in the binary 0 state (**bR**) absorb the 690nm light, because these elements have cycled into the **O** state. Noting that all of the volumetric elements outside of the paged area are restricted to the **bR**, **P** or **Q** states, the only significant absorption of the beam is associated with **O** states within the paged region. The CCD detector array therefore observes the differential absorptivity of the paged region, and the paged region alone. This selectivity is the key to the read operation, and it allows a reasonable signal-to-noise ratio even with thick (1–1.6 cm) memory media containing $>10^3$ pages. Because the absorptivity of the **O** state within the paged region is more than 1000 times larger than the absorptivity of the remaining volume elements combined, a very weak beam can be used to generate a large differential signal. The read process is complete in ~10 ms which gives a rate of 10 MB/s. Each read operation must be monitored for each page, and a refresh operation performed after ~1000 reads. While data refresh slows the memory slightly, page caching can minimize the impact.

C. Data can be erased by page or globally.

In our previous (Level I) prototype, we used a Krypton-ion laser operating at 413 nm to erase single pages at a time. Our current prototype (Level IIA) is designed to test the potential of using commercially available diode lasers, but here we have a problem. At present, there are no readily available blue diode lasers, although a number of companies are working on developing these lasers. In the interim, we are using a filtered quartz-halogen lamp (QHL in Fig. 4A) to provide the blue light for erasure. By choosing an incandescent source, any hope of single page erasure is lost, and now we must be satisfied with multiple page erasure. For the time being, we accept this constrained, anticipating that blue diode lasers will be available in the near future.

The optimal wavelength for erasing data is ~410 nm, because this wavelength will photoconvert both **P** and **Q** back to **bR** (scheme 1 & Fig. 6). Alternatively, one can clear an entire data cuvette by using incoherent light in the 360 – 450 nm range. The latter option may prove useful for some commercial implementations. A broad-band data clear operation must be carried out in the absence of red light, however, because blue light can activate the photocycle and produce the **O** state. As long as the erasing light is not absorbed appreciably by the **O** state, however, a sufficient population of the **P** and **Q** molecules (bit 1) will be reset to **bR** (bit 0).

As an aside, it is interesting to consider whether a clear operation should be implemented at all. The cost of a data cuvette is relatively small. As noted below, we use inexpensive plastic cuvettes and the amount of protein that is required to make a single cuvette capable of storing hundreds of megabytes is on the order of milligrams. Because the protein can be produced in mass quantities by using fermentation technology not much different from making beer, some investigators have proposed that the memory be implemented as a WORM device (write once-read many times). An inexpensive bulk eraser device using incoherent blue light could be provided for those wishing to re-use data cuvettes.

D. Preparation of the data cuvette.

Bacteriorhodopsin (BR) is isolated from the bacterium *Halobacterium halobium* (also called *Halobacterium salinarium*) in the form of purple membrane sheets, which consist of the protein suspended in a lipid membrane. Our current strain of *H. halobium* is a variant of S9-P, an enhanced overproducer of bacteriorhodopsin, which is isolated via well-defined procedures described in the literature [22,26]. Purple membrane sheets are suspended in distilled water and stored at 4°C until ready for use. Prior to use, the concentration of BR is adjusted to 10-20 mg/ml.

The cubes used in the branched photocycle volumetric memory are produced by suspending purple membrane in a polymer matrix. The matrix must be sufficiently rigid to encapsulate the membrane and trap it in place, while providing enough moisture to ensure that bacteriorhodopsin retains its full activity. It also must provide a high degree of optical clarity and homogeneity for proper functioning of the optical memory. The polymer matrix must be rigid enough to prevent protein migration, but flexible enough to permit the protein to undergo modest changes in volume that take place during the photocycle. Although we are still looking for improved polymer matrices, to date poly(acrylamide) has shown the most promise.

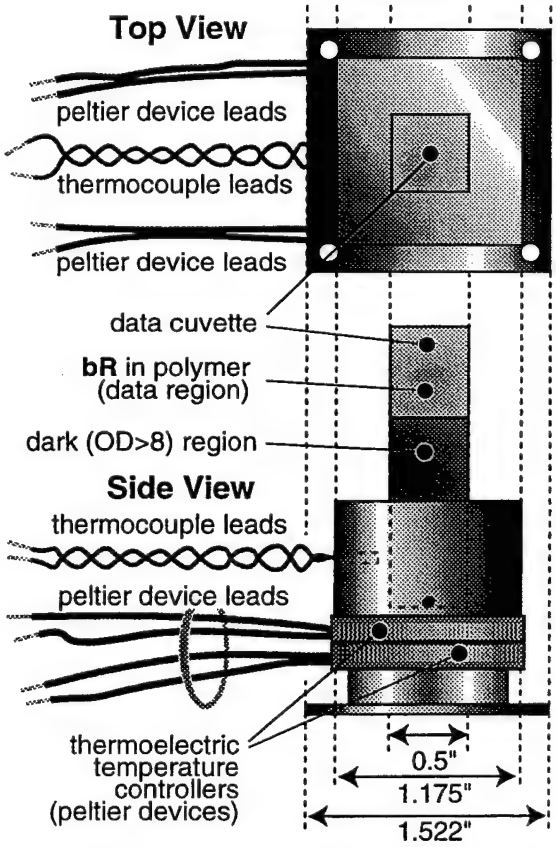

Figure 7. Schematic diagram of the protein data cuvette and holder.

Fabrication of bR-based optical cuvettes (Fig. 7) is accomplished by in situ polymerization of the acrylamide-bR solution. Concentrated purple membrane is added drop-wise to a small volume of 10 % (wt/vol) acrylamide (~2 ml) until the optical density at 570 nm reaches 2-3 absorbance units. The resulting solution is then filtered (5 μ, syringe-type) and sonicated for 1-2 minutes (prolonged sonication can result in vesicle formation, inadequate sonication generates a polymer with too much scattering). At this point the solution is degassed for several minutes, because dissolved oxygen can inhibit the acrylamide polymerization process. Fresh ammonium persulfate solution [$(NH_4)_2S_2O_8$,

1.5% aqueous, w/v)] is added to initiate and catalyze polymerization, followed by a small volume of TEMED (N, N, N', N'-Tetramethyl-ethylenediamine) to act as an accelerator of the polymerization process. The volumes of these two reagents are typically on the order of 75 μL and 10 μL, respectively, per mL of 10% acrylamide. The solution must be quickly mixed and transferred to a standard fluorescence cuvette before polymerization is fully accelerated; failure to do so will result in optical distortions within the matrix (flows and eddies due to differing rates of polymerization). The rate of polymerization is largely controlled by the concentrations of ammonium persulfate and TEMED. The volumes of these reagents can therefore be adjusted to minimize formation of optical defects in the cube. The total volume of acrylamide/bR solution needed is approximately 1.5 ml.

The acrylamide solution is prepared to be 10% T and 5% C, where T represents the total monomeric concentration of acrylamide, and C represents the concentration of cross-linking agent (bisacrylamide). Addition of a cross-linking agent enables the formation of an actual gel, as opposed to a viscous solution of long polymer chains which would be incapable of encapsulating the purple membrane fragments. The relative proportions of T and C are crucial to the ultimate optical quality of the gel, especially with respect to light scattering. The concentration of cross-linking agent controls the effective pore size, and is generally within the range of 2.5 - 5% (pore size of approximately 20 nm). Addition of too much bisacrylamide (relative to acrylamide) leads to enlarged pore diameters (several hundred nm) and a consequent increase in light scattering [27].

After the cube has gelled, a second acrylamide layer is added. The purpose of this layer is two-fold: primarily, it aids in the reduction of light scattering and reflection which might interfere with the reading and writing processes, and secondly it acts as a filler for the rest of the cuvette, which is then sealed to ensure that it is air-tight. The protocol for fabrication of this layer is as described above, except that enough bR is added so that the solution appears black: deeply colored laser dyes were originally attempted for this purpose, but preliminary studies indicated that they interfered with the polymerization process. The cuvette is filled to about two thirds of its total volume, and is made air-tight by the use of either silicone sealants or a UV-curable optical adhesive. A custom-made base for the cube facilitates permanent sealing of the cuvette, as well as temperature regulation via peltier coolers. The cube base is illustrated in Fig. 7. The cuvette is inserted into the holder, which is equipped with ports for insertion of thermocouples which monitor the temperature and indirectly control the peltier coolers.

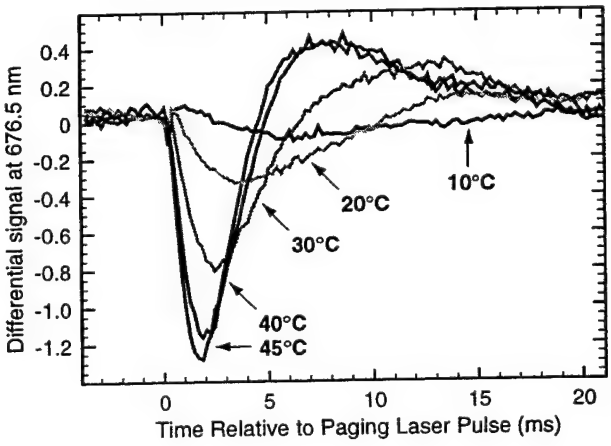

Figure 8. The effect of temperature on the magnitude and the decay time of the differential read signal.

E. The effect of temperature.

Our studies indicate that the signal-to-noise ratio of the read process is highly dependent upon temperature. Furthermore, the probability of writing a one bit is enhanced

by increasing the temperature. Both factors are associated with the effect of temperature on the formation of the **O** state. The key experimental results are shown in Fig. 8. The downward peak is associated with the formation of the **O** state, and the consequential absorption of the 676.5 nm beam by this state. (We note that our present prototype uses a 690nm diode laser, but the data shown in Fig. 8 are relevant to any read operation in the 650 - 700 nm region.) The rise time is associated with the decay of the **O** state, but the fact that it "over shoots" the zero level is due to capacitive effects in the detector array (we are working to eliminate this problem). Note that the intensity of the negative signal as well as the decay of the signal increases with increasing temperature. This observation can be explained by reference to the detailed kinetic analyses of the photocycle carried out by Varo and Lanyi [28,29]. The signal to noise ratio of the read process is proportional to the magnitude of the negative signal divided by the magnitude of the signal fluctuation in the time segment from -2 to 0 ms. The worst-case S/N ratios for the read process as a function of temperature are as follows: 1.5 (10°C), 3 (20°C), 8 (30°C) and 11 (40°C). Other sources of error become dominant in producing read errors at temperatures above 30°C, and hence we have adopted this temperature as the nominal operating temperature of the data cuvette. As noted previous, the temperature of the cuvette is controlled by using thermoelectric heaters (see Fig. 7).

Temperature also affects the timing of the write and read data beams. For optimal writing, the on and off times are given by the following equations,

$$\Delta t \text{ (data beam on)} = 21.8 \text{ ms } T_c(°C)^{-0.7} \qquad (10°C < T_c < 45°C) \qquad (1)$$

$$\Delta t \text{ (data beam off)} = 61.1 \text{ ms } T_c(°C)^{-0.7} \qquad (10°C < T_c < 45°C) \qquad (2)$$

where Δt is the time in milliseconds relative to address beam activation and T_c is the temperature of the memory cuvette in degrees Centigrade. The above relationships are approximate and are limited to pH=7 solution or well humidified polymer environments. The data beam on time is equal to the time at which the signal curve if Fig. 8 reaches half of its minimum value. The data beam off time is equal to the time at which the signal returns to its half-minimum value. These times are appropriate for both the read and write data beam timings, but as noted above, the read process is carried out by using a very low light level. Examination of Eqs. 1 and 2 indicates that the memory can operate more rapidly at higher temperatures, but temperatures above 40°C should be avoided as elevated temperatures decrease the cyclicity of the protein.

F. Reliability

As noted in our previous progress report (RL-TR-96-274), the key goal of the present contract was to improve upon the reliability of the read operation. This has been accomplished, as shown in Fig. 9. Note that the overlap region has become much smaller relative to the integral under the correct main bit 0 and bit 1 curves. If the assignment level is set at the arrow in each example, the error associated with the read process is minimized. In the following discussion, we provide a detailed discussion of the methods and procedures of calculating read error rates from the read histograms.

Figure 9. (next page) Histograms of bit intensities during read operations for the previous Level I prototype (top graph) and present Level IIA prototype (middle and bottom graphs).

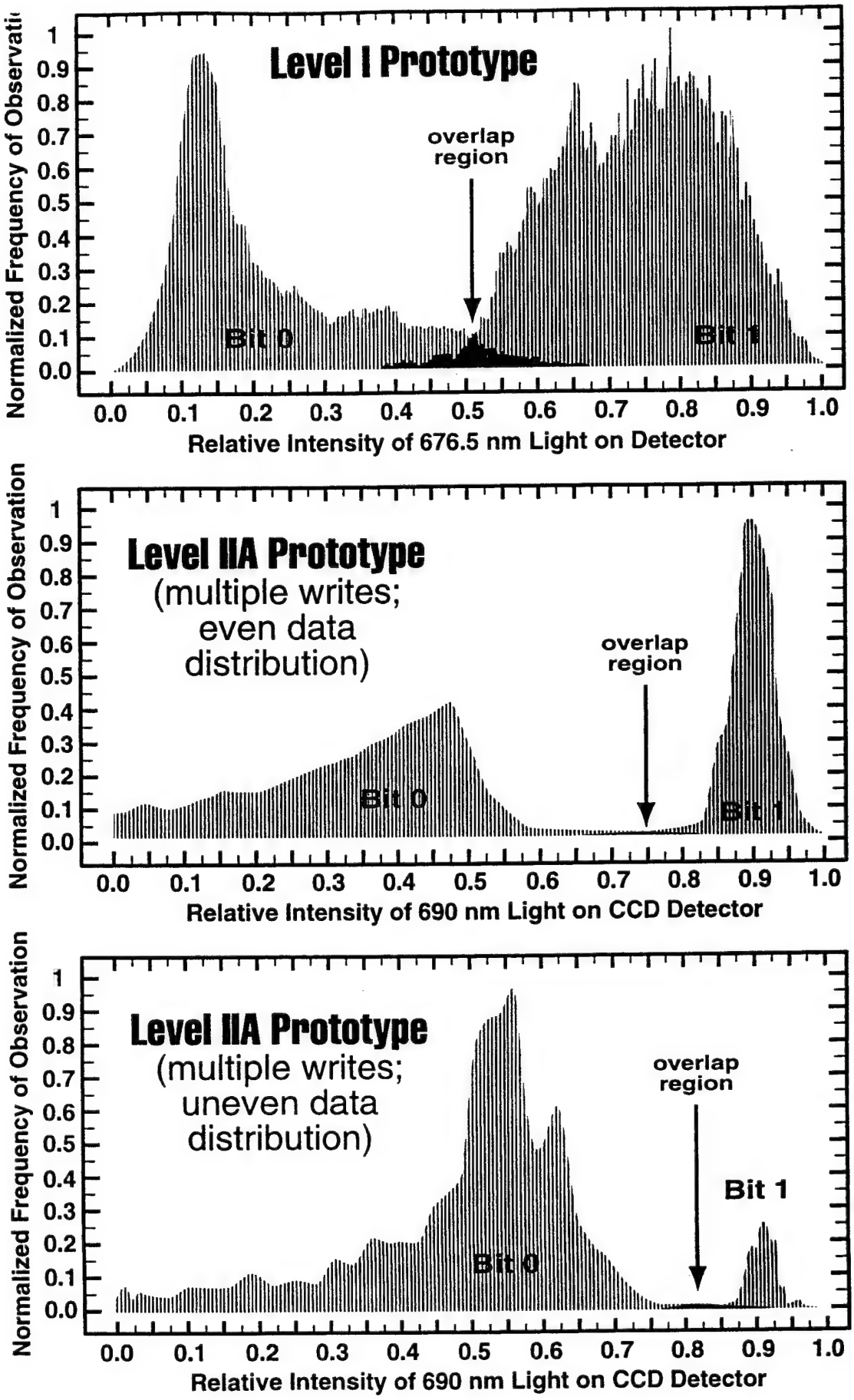

Figure 9 (Caption on previous page)

Calculation of Reliability from Read Histograms. The improvement in the reliability of our Level IIA prototype is sufficient to warrant a more detailed discussion of this issue, and how one can use the data presented in Fig. 9 to calculate the probability of a read error. We note at the outset that we place all of the error into the read portion of the process, although the error could be due entirely to an imperfect write operation. For the purposes of analysis, however, the error does not show up until one tries to carry out a read operation, and thus it is more useful to analyze error entirely in terms of "read error".

The process of assigning the state of a bit during the read process is based on the measurement of the intensity of light passing through that microscopic portion of a page upon which the bit has been written. In this discussion, we assign Bit 0 to the **bR** molecule and Bit 1 to the **P/Q** states. Thus, Bit 0 is assigned based on the preferential absorptivity of the **O** state (for details, see Figs. 5 and 6 and related discussion). Naturally, we could reverse the bit assignments without affecting the reliability, and there may be some instances when such a reversal would be useful. At this stage, we also neglect reliability enhancement associated with the addition of error correcting bits. This will be the subject of the final paragraph of this section.

Whether a given location is assigned to Bit 0 or Bit 1 is determined by a threshold level called the "bit assignment crossover point", and represented by the symbol, ζ. The optimal value is determined by carrying out a reliability analysis on the assignment of both bits, under the assumption that one seeks a point which minimizes the error in arbitrary assignments. In other words, the error is minimized for simultaneous assignments of both bits 0 and 1 within a given page. To understand the process, and the assignment of error, in more detail, we provide the analyses presented in Figures 10 and 11.

Our first example assumes identical Gaussian distributions for bit response functions based on a normalized response function, ξ, from 0.0 to 1.0 (see Fig. 10, top). The error in the read process is numerically assigned by defining the following integrals:

$$A_0 = \text{integral under Bit 0 read histogram} = \int_0^1 B_0[\xi]d\xi \tag{1}$$

$$A_{0x} = \text{Bit 0 error integral} = \int_\zeta^1 B_0[\xi]d\xi \tag{2}$$

$$A_1 = \text{integral under Bit 1 read histogram} = \int_0^1 B_1[\xi]d\xi \tag{3}$$

$$A_{1x} = \text{Bit 1 error integral} = \int_0^\zeta B_1[\xi]d\xi \tag{4}$$

$$A_{01} = \text{integral under Bit 0 and Bit 1 overlap regions} = \int_0^1 B_{01}[\xi]d\xi \tag{5}$$

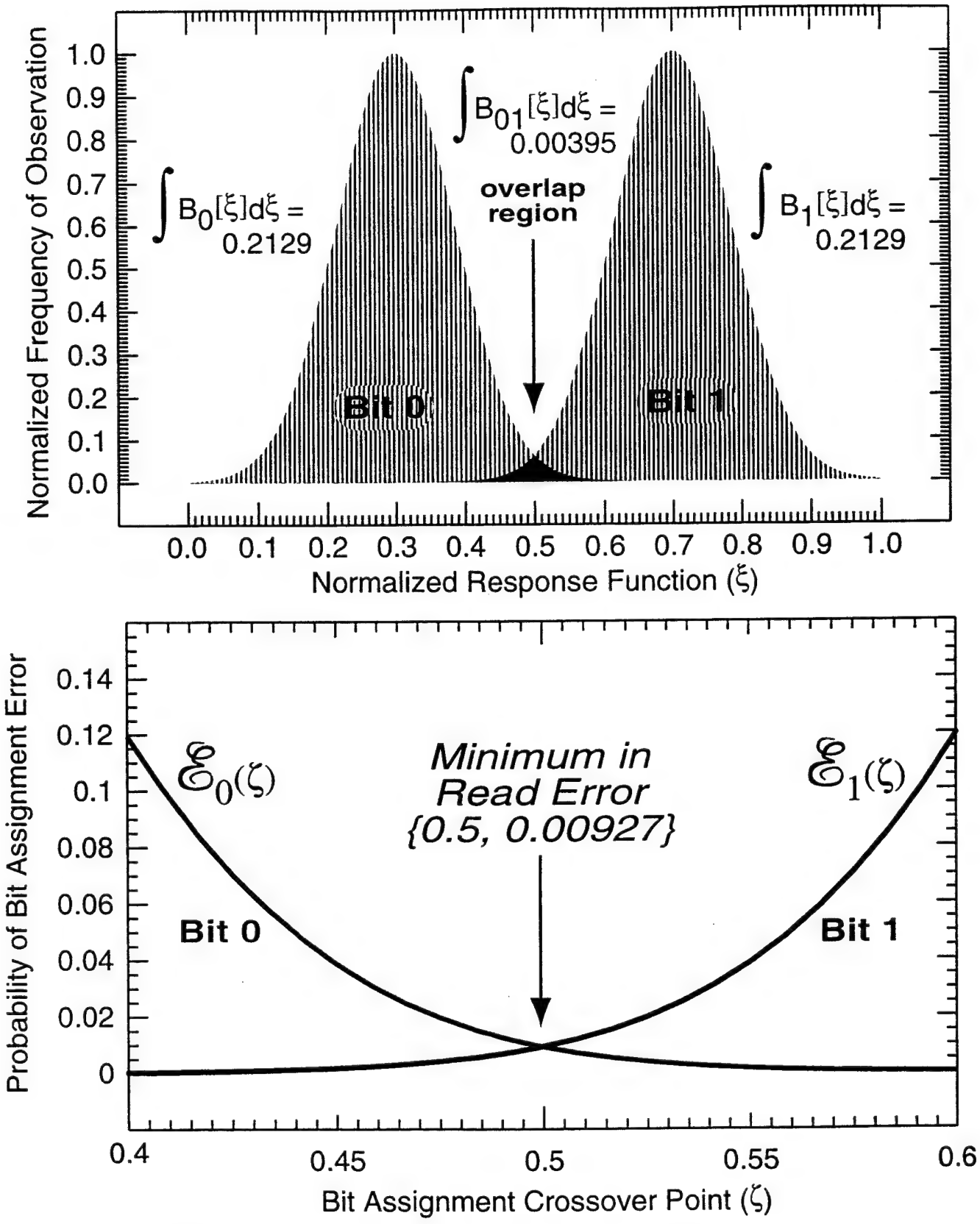

Figure 10. Error analysis for two identical overlaping Gaussian distributions.

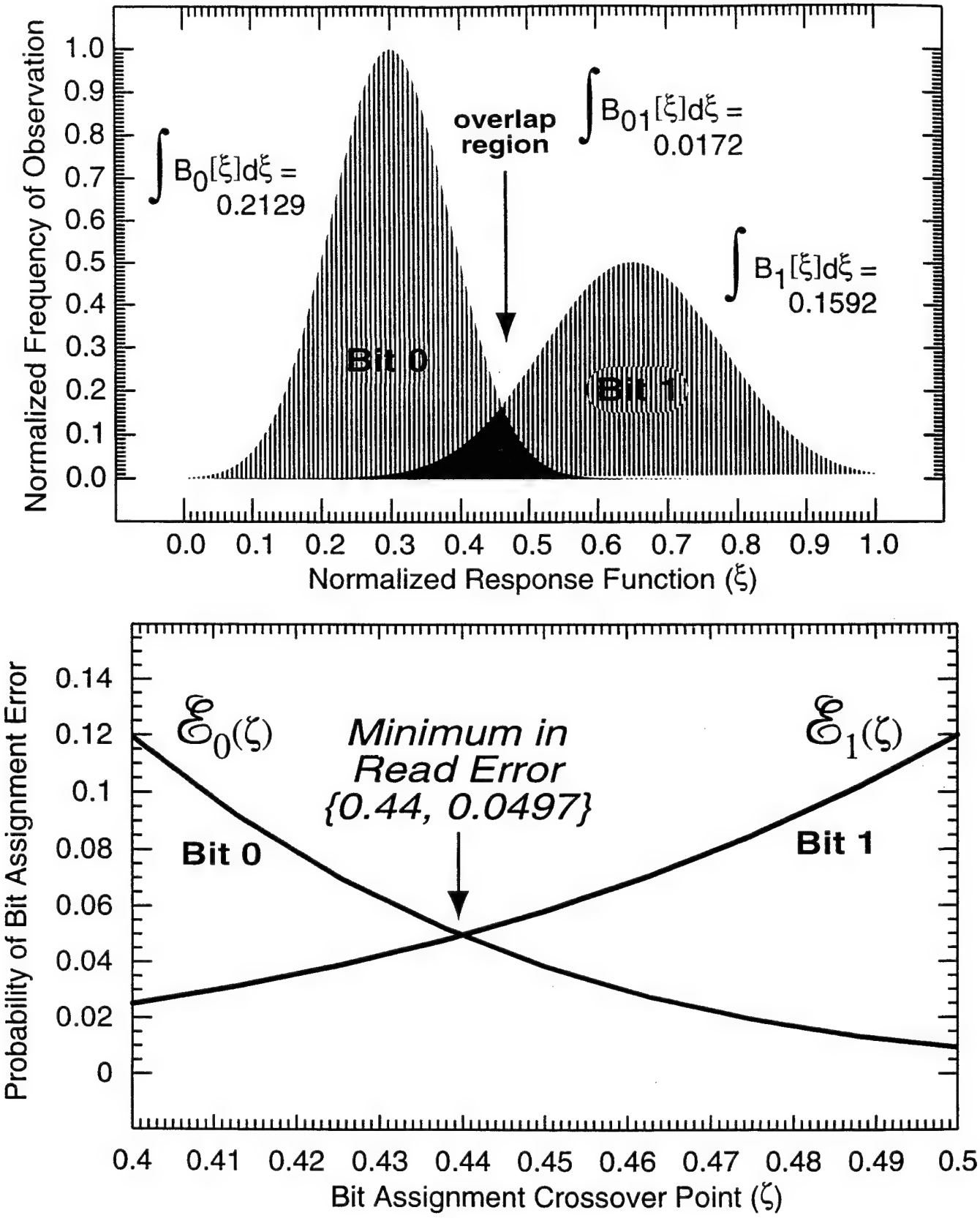

Figure 11. Error analysis for two different overlaping Gaussian distributions.

In the example shown in Fig. 10, we have chosen arbitrarily a full-width at half-maximum that produces an overlap in the read histograms (distributions). This overlap region generates error, because a read operation that returns a value for the response function within this region is ambiguous. The ambiguity can be minimized by judicious choice of the threshold value, ζ, but never eliminated completely.

The error in reading Bit 0, $\mathscr{E}$, (as a function of ζ) is:

$$\mathscr{E}_0(\zeta) = \text{error in Bit 0 read process} = A_{0x}/A_0 \tag{6}$$

with a similar equation defined for Bit 1:

$$\mathscr{E}_1(\zeta) = \text{error in Bit 1 read process} = A_{1x}/A_1 \tag{7}$$

The optimal value for the bit assignment threshold (or crossover point) is given by that value of ζ for which $\mathscr{E}_0(\zeta) = \mathscr{E}_1(\zeta)$. This approach is shown graphically in Fig. 10, bottom, and in the case of the two symmetric Gaussians, yields $\zeta = 0.5$ and a read error of $\mathscr{E}_0(\zeta{=}0.5) = \mathscr{E}_1(\zeta{=}0.5) = 0.00927$. This means that there is a 0.9% chance of an incorrect bit assignment during a single read process. If one reads a page of data comprising 1024×1024 = 1,048,576 bits, 9720 bits will be missassigned. This is clearly unacceptable, but as noted below, the use of error correcting bits modifies the situation significantly.

The reader may wonder how much math is actually involved in analyzing the equality, $\mathscr{E}_0(\zeta) = \mathscr{E}_1(\zeta)$, as a function of ζ. Unfortunately, such calculations normally require numerical methods, which are quite cumbersome and a powerful workstation is required if a large error histogram data base is being used. If the histograms can be fit to Gaussians, the following pseudo-closed-form expressions can be used to calculate the integrals:

$$\text{Let } B[\xi] = \exp\left(\frac{-c_1\,(x - x_0)^2}{\Delta x^2}\right),$$

where c1 is a constant (-4*ln(2)) yields normalized distributions), x_0 is the center of the Gaussian distribution and Δx is the full-width at half-maximum. The general integral, from *a* to *b* within the normalized response function can be calculated using the expression,

$$\int_a^b B_0[\xi]d\xi = \frac{\Delta x\,\pi^{1/2}\,\mathrm{erf}(c_1{}^{1/2}\,\Delta x^{-1}\,(b - x_0))}{2\,c_1{}^{1/2}} - \frac{\Delta x\,\pi^{1/2}\,\mathrm{erf}(c_1{}^{1/2}\,\Delta x^{-1}\,(a - x_0))}{2\,c_1{}^{1/2}}$$

where "erf" is the error function. This function is normally provided in newer implementations of FORTRAN and C and is a built-in function in Mathematica and Maple. If this function is not available, one is better off doing numerical integration using the raw histogram file. It should further be noted that normalization of the histogram data is not required for the above functions to work. Normalization is automatically provided by Eqs. 6 and 7. It is however important that the Bit 0 and Bit 1 histograms be scaled the same amount, if scaling is being carried out. We use normalized data solely for the purposes of plotting.

Given the computational complexity of using trial and error methods to solve $\mathscr{E}_0(\zeta) = \mathscr{E}_1(\zeta)$, we mention a simple method of estimating the minimum error without assigning ζ. This method only requires integration of the overlap region and ratioing of that integral to the integrals under the 0 and 1 bit histograms:

$$\mathscr{E}_{01} = \frac{A_{01}}{A_0 + A_1} \tag{8}$$

If the data are perfectly symmetrical, this estimate is identical to the calculated value based on solution of the $\mathscr{E}_0(\zeta) = \mathscr{E}_1(\zeta)$ equation. For example, the data in Fig. 10 yield 0.00927 based on simultaneous minimization of the $\mathscr{E}_0(\zeta)$ and $\mathscr{E}_1(\zeta)$ and Eq. 8 gives the same result,

$$\mathscr{E}_{01} = \frac{A_{01}}{A_0 + A_1} = \frac{0.00395}{0.2129 + 0.2129} = 0.00927$$

Although the above $\mathscr{E}_{01}$-based method works well for error calculations involving symmetric distributions (identical but shifted bit 0 and 1 histograms), this method is not rigorous when uneven distributions are analyzed. As shown in Fig. 11, an unsymmetrical overlap region requires the explicit evaluation of the $\mathscr{E}_0(\zeta)$ and $\mathscr{E}_1(\zeta)$ functions to rigorously determine the error. In particular, Eq. 8 yields 0.0462 for the estimated error (see data in top graph of Fig. 11) compared to a more rigorous value of 0.0497 (bottom of Fig. 11).

Reliability analyses on the previous and current prototypes are summarized in Figs. 12-14. The results are tabulated below:

Prototype	Bit Distribution	Optimal ζ	Minimum Error	Fig. No.
Level I	roughly even	0.524	0.044	12
Level IIA	roughly even	0.768	0.009	13
Level IIA	more 0's than 1's	0.744	0.011	14

We note that while the error has improved by a factor of at least four, the read error is still relatively high and would preclude commercialization, if further improvement were not possible. For reference, we note that the simple $\mathscr{E}_{01}$-based error calculations yield values of 0.041, 0.009, and 0.007 for the three cases shown in Figs. 12, 13 and 14, respectively. Thus, the simple error calculation breaks downs significantly when uneven bit distributions are encountered. Of greater importance to the implementation of the memory is the observation that the optimal bit assignment threshold, ζ, shifts in value when the ratio of 0 to 1 bits changes. This observation may require that the data for each page be manipulated to maintain a more even distribution, which is certainly possible, but rather undesirable. An alternative is to use gray scale recording which enhances both data storage density and helps to even out the distribution. Much remains to be done before gray-scale recording is possible, however.

In closing, we note that the addition of error correction bits dramatically improves reliability. For example, by using two error-correcting bits for each 8-bit byte of binary data, one achieves single bit error correction and double bit error detection. By using a 10-bit byte, therefore, we can decrease the probability of a catastrophic read error for a byte of information from ~8% (0.01*8) to less than 0.6%. Clearly, error correction helps, but not enough to transform our present level of reliability into commercial viability. More work is needed (see Section 7 below).

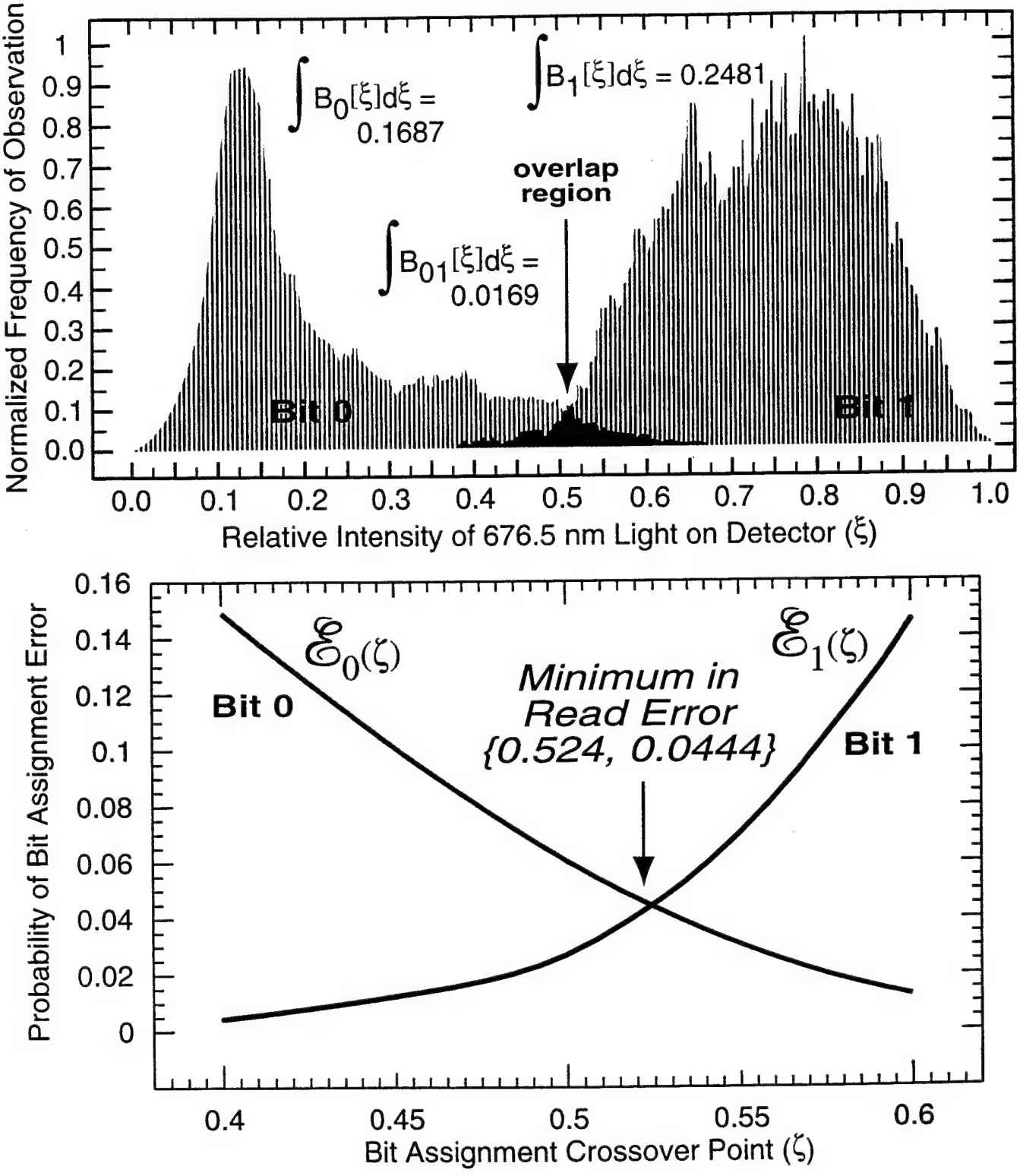

Figure 12.
Read error analysis for the level I prototype developed as part of the previous research contract for data sets involving roughly equal numbers of 0 and 1 bits.

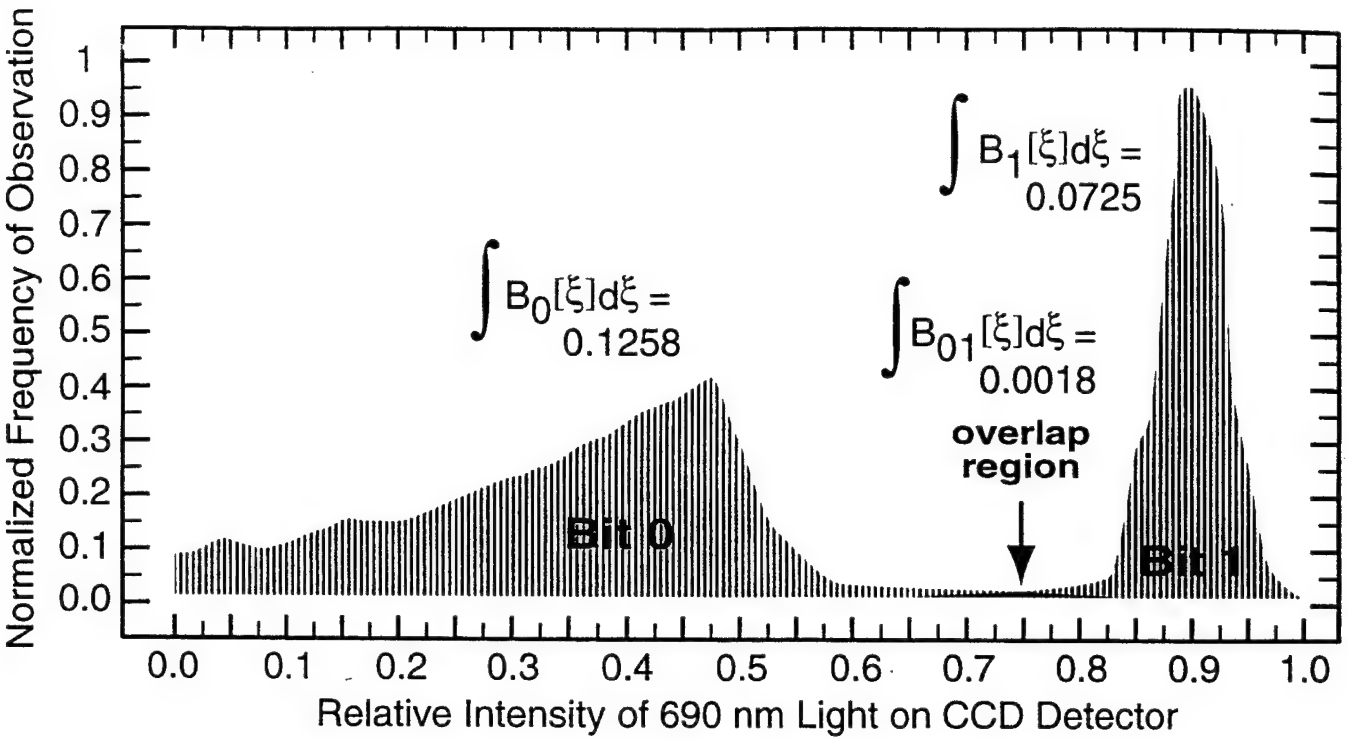

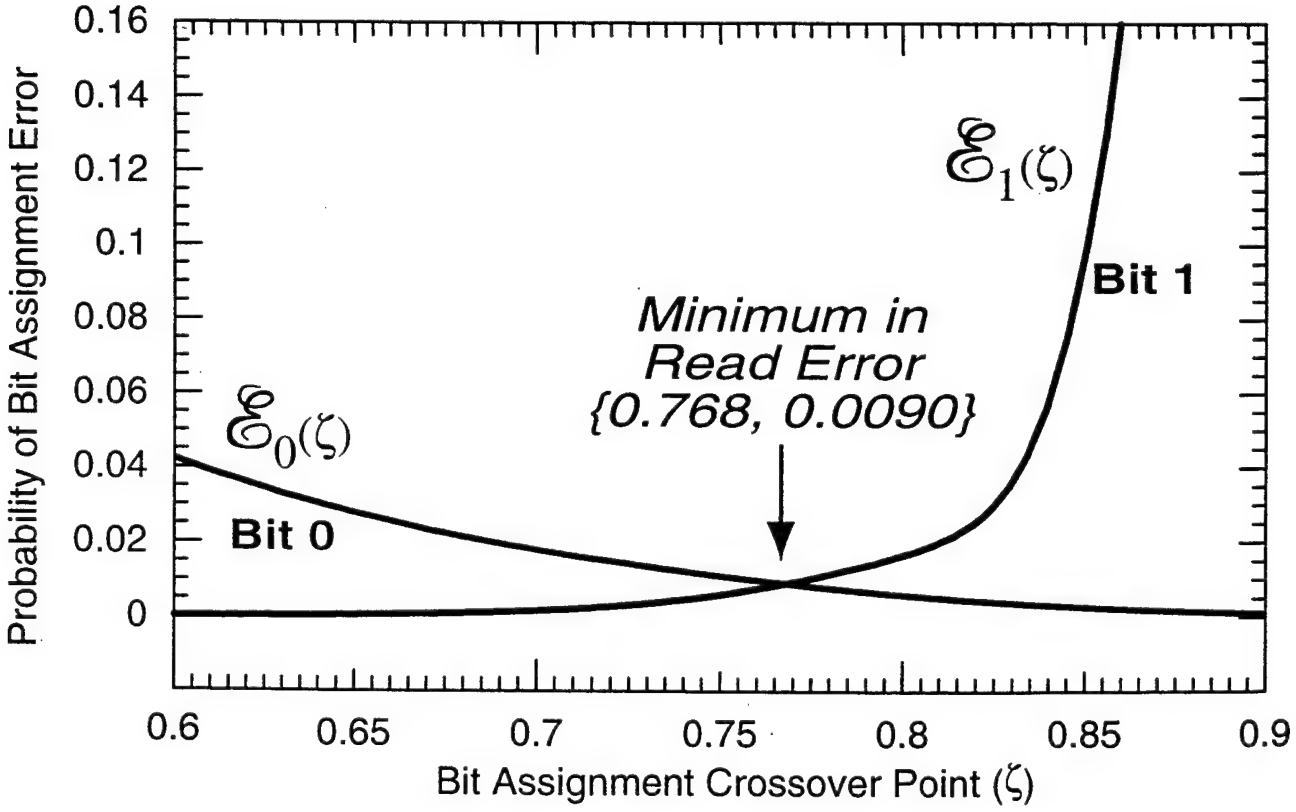

Figure 13.
Read error analysis for the level IIA prototype developed as part of this research contract for data sets involving roughly equal numbers of 0 and 1 bits.

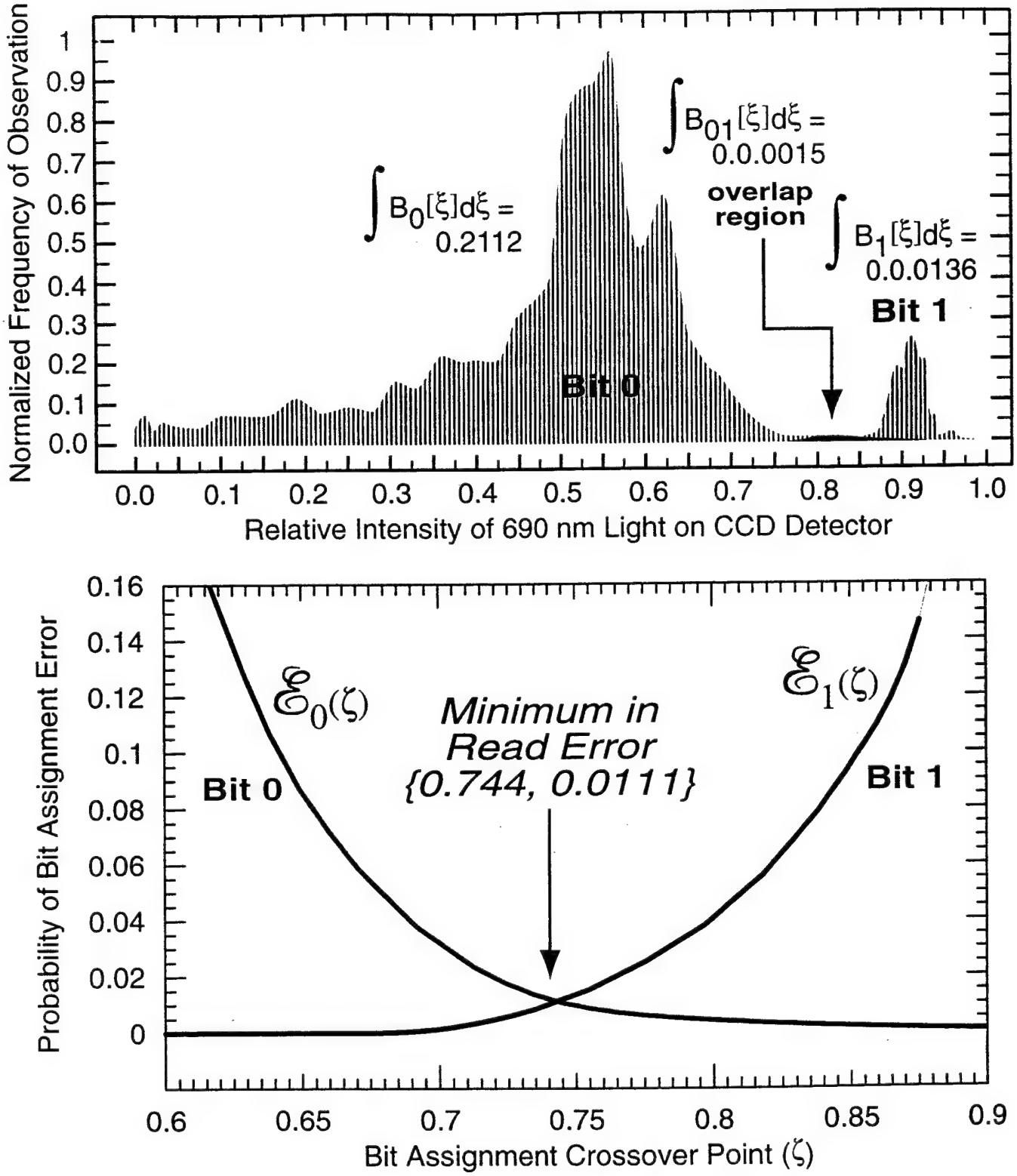

Figure 14.
Read error analysis for the level IIA prototype developed as part of this research contract for data sets involving significantly more 0 bits than 1 bits.

5. Protein Modifications to Improve Memory Performance.

The storage of data using **P** and **Q** states is linked directly to **O** state yield, and we have been studying both chemical and genetic methods of improving this variable. Most of this work was carried out during the previous contract, and we summarize the current state of knowledge here. One promising approach is site directed mutagenesis, and in particular, the replacement of leucine 93 with tyrosine or the replacement of glutamic acid 204 with a non carboxylate amino acid [30-32]. These single amino acid substitutions greatly increase the yield of the **O** state, but they also increases the lifetime of the **O** state, which slows down the cycle time of the memory. Other mutants are under study. This section will concentration on a discussion of organic cation protein analogs, a few of which yield a five-fold improvement in protein performance.

It has long been known that the functioning of light–adapted bacteriorhodopsin ($\lambda_{max} \approx 570$ nm) as a proton pump requires the presence of Ca^{2+} and Mg^{2+} ions which bind at specific locations inside the protein and on the surface [22]. Approximately 3-5 divalent cations are bound to the protein, although the mechanism of the binding remains a subject of debate [33]. Removal of these cations produces what is called the blue membrane ($\lambda_{max} \approx 605$ nm), a protein with a truncated photocycle incapable of vectorial proton pumping. The spectroscopic and photochemical properties of the protein can be restored fully by adding either calcium or magnesium to an aqueous solution of the blue membrane [22,33]. The second high-affinity binding site is primarily responsible for the blue to purple transition [34]. Recent two-photon experiments indicate that this binding site, hereafter referred to as the chromophore-adjacent cation binding site, involves the participation of ASP_{85} and ASP_{212} along with additional stabilization from TYR_{57} and TYR_{185} [22]. This model of the binding site is shown in the bottom diagram of Fig. 3.

We have observed that analog proteins with nearly identical spectroscopic properties and similar photochemical properties can be generated by adding large organic monovalent and divalent cations to the blue membrane [35]. A selection of some of the organic cations that we have studied with respect to protein performance related to the three-dimensional memory are shown in Fig. 15. The spectra of the organic-cation bR analogs are similar to the native protein with absorption maxima within a few nanometers of the native protein. In order to examine systematic variations, the main absorption bands of the protein spectra were fit by using a log-normal distribution function. This procedure fits the band to a skewed Gaussian as a function of the absorption maximum (λ_{max}), full-width-at-half-maximum ($\Delta\tilde{\nu}$) and skewness (σ). The results of the least-squares fits are shown in Fig. 15 for spectra recorded in polyacrylamide gel (the polymer used to make the data cuvettes). As we demonstrate below, the modest shift in absorption spectra do not fully reveal the large changes that were observed in the **O** state kinetics.

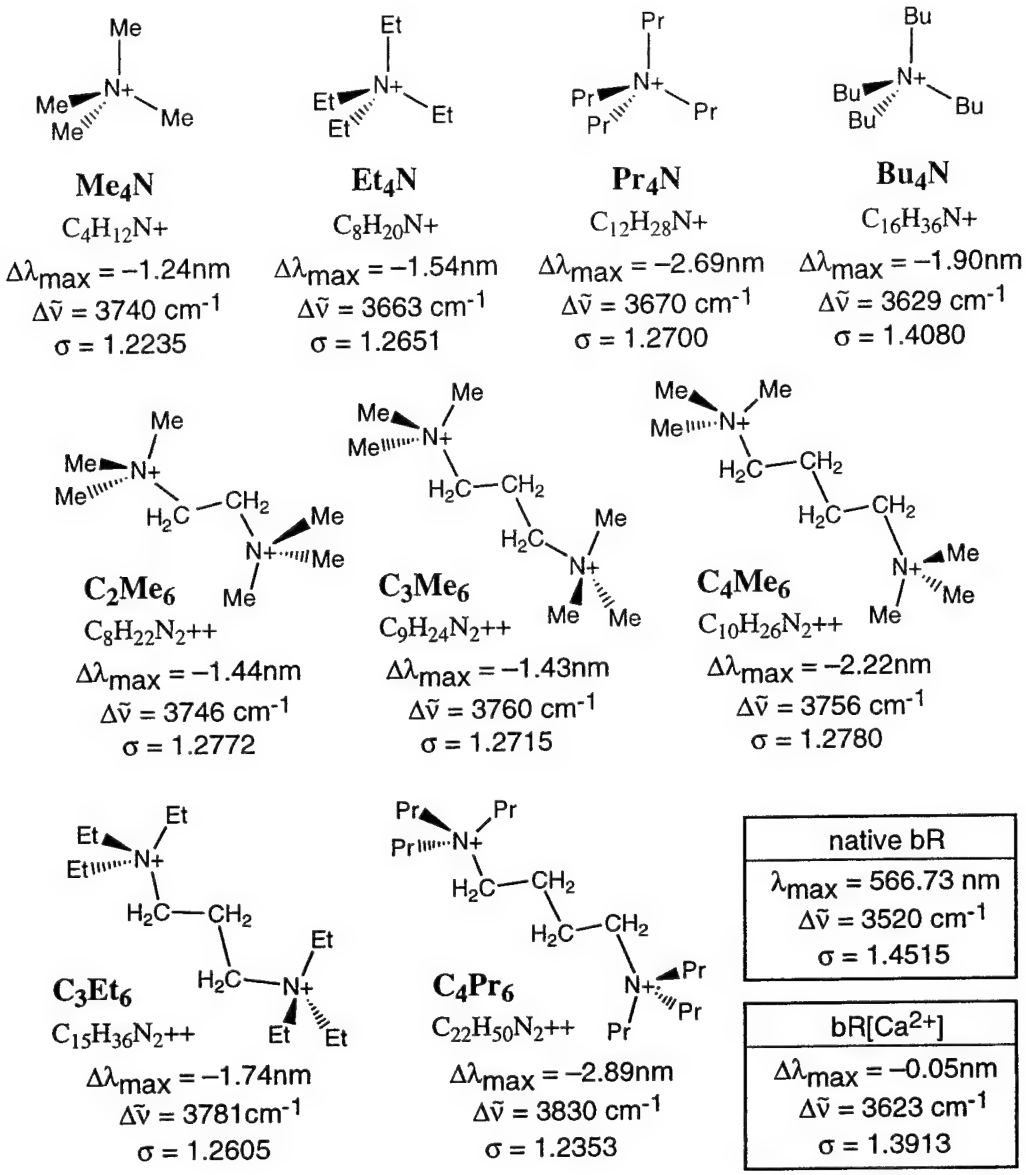

Figure 15. Structure of the quaternary ammonium cations and the spectroscopic properties of the light-adapted analog proteins generated via addition of the organic cations to the blue membrane of bacteriorhodopsin.

A. Preparation of the organic cations.

The dibromoalkanes and trialkyl amines were purchased from Aldrich (cat. nos. 24,065–6, 12,590–3 and 14,080–5) and Fluka (cat. nos. 92260, 90342 and 93240) respectively and were used as received. Acrylamide, N,N'–methylene–bis–acrylamide, azolectin, tris(hydroxymethyl)aminomethane (Tris) and EDTA were purchased from Sigma (cat. nos. A–8887, M–7279, P–7443 ,T–1503 and EDS respectively) and were used without further purification. Ammonium persulfate and $CaCl_2.2H_2O$, purchased from Fisher (cat. nos. A682–500 and C–79 respectively) were of pure grade. Iodomethane and tetramethylethylenediamine were purchased from Aldrich (cat. nos. 28,956–6 and 41,101–

9 respectively) and were used as received. Distilled and deionized water (Barnstead E–pure) was used throughout the experiments.

The divalent 'bolaform' cations [$\mathbf{C_nR'_6}$ where n is the number of carbon atoms in the alkyl chain attached between the two quaternary ammonium groups and **R'** references the six identical hydrocarbon groups attached to the two nitrogen atoms, **R'** = CH_3 (**Me**), C_2H_5 (**Et**) or C_3H_7 (**Pr**)] were synthesized from the appropriate dibromoalkane by using the following reaction to form the desired n–alkane–α,ω–bis(trialkylammonium)dibromide:

$$Br(CH_2)_nBr + 2\,\mathbf{R}_3N \xrightarrow[\text{reflux ~3hrs.}]{\text{MeOH}} Br\mathbf{R}_3N(CH_2)_n\mathbf{N}R_3Br \qquad \text{(scheme 2)}$$

where n = 3 or 4 and **R** = CH_3 (**Me**), C_2H_5 (**Et**) or C_3H_7 (**Pr**). The details of the preparation follows a standard method [36]. A two–fold excess of the trialkylamine of choice is added to a methanolic solution of the dibromoalkane and refluxed for about three hours. The product, which is precipitated upon cooling the solution, is filtered off and washed three times with cold methanol. The supernatant is partially evaporated by using a rotary evaporator and a few drops of ether is added before the solution is chilled to form a second batch of the product. The crude product is recrystallized three times from methanol to produce the pure, white–crystalline powder. We discovered, however, that the above procedure is not applicable to the preparation of $\mathbf{C_2Me_6}$. The NMR spectrum revealed displacement of only one of the bromides of 1,2–dibromoethane by trimethyl ammonium. Thus, $\mathbf{C_2Me_6}$ was prepared by the following procedure. A slight excess of methanolic iodomethane is added dropwise into a methanolic solution of tetramethylethylenediamine. The mixture is left to stand for ~1 hour. The crude product which precipitates is filtered off, washed three times with cold methanol and recrystallized three times from methanol to yield the desired white–crystalline product.

B. Photophysical properties of the organic cation analog proteins.

Although the organic cations have an impact on a number of the photophysical properties of the protein, we will concentrate on an analysis of only two properties relevant to this contract. The first is cyclicity, or the number of times the protein can be cycled from the resting state (**bR**) to the branched states (**P & Q**), and then back again to **bR**. The number for the native protein is about 10^5, which means the native protein under normal applications, will function for about five years of normal use. All of the organic cation analogs appear to have a comparable cyclicity with the exception of the large monovalent cation analogs such as $\mathbf{Bu_4N}$. The latter has a cyclicity of about 10^3, which is unacceptable. We believe the latter cation is too large to fit inside the cation binding site without disturbing the location of the membrane spanning helices. In the process, the protein is destabilized, which limits the number of times the protein will undergo a photocycle prior to denaturation.

The key property provided by some of the organic cations involves the lifetime and the yield of the **O** state. The experimental results are shown in Fig. 16.

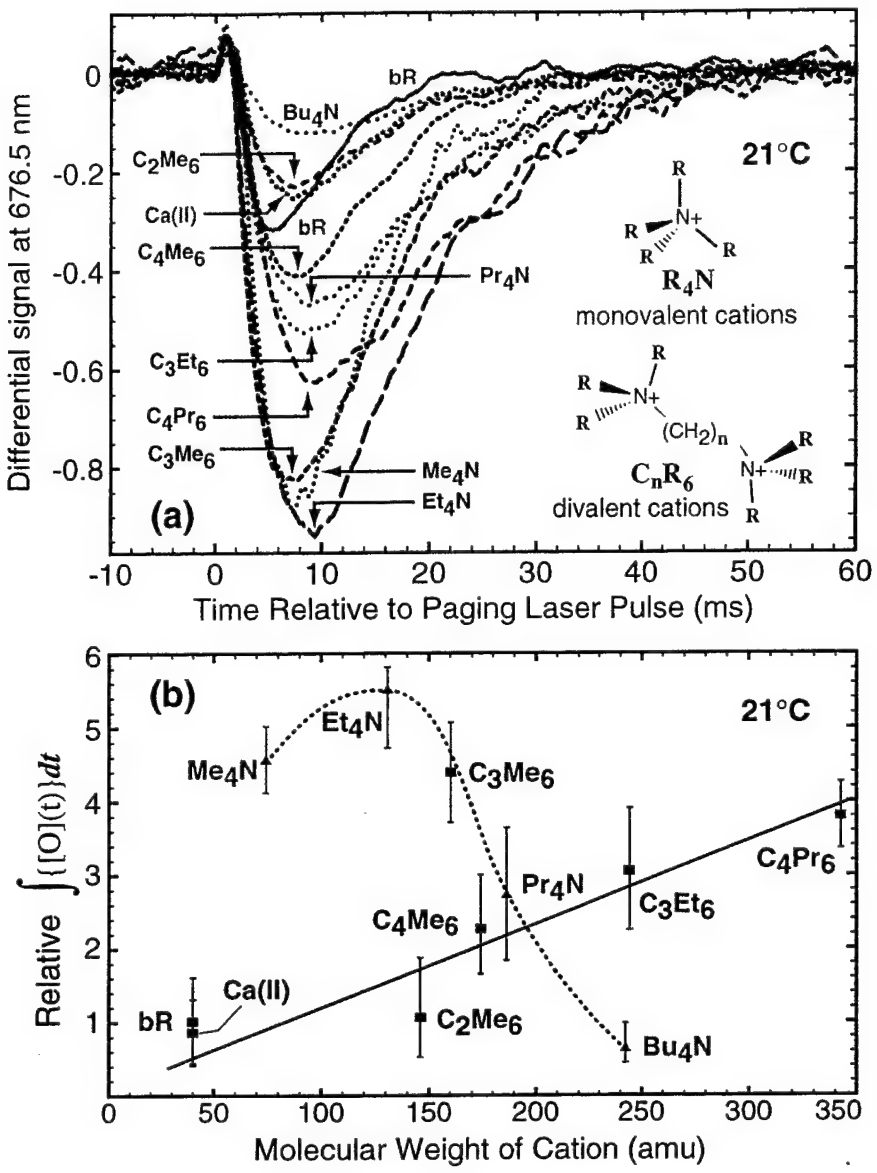

Figure 16. The influence of organic cation size and structure on the formation, decay and yield of the **O** state. Some organic cations enhance significantly the yield and the lifetime of the **O** state. The efficiency of photogenerating the **P** state from the **O** state (i.e., writing bit 1) is proportional to the integral of **O** concentration with respect to time, which is graphed as a function of the cation molecular weight in (b).

The results shown in Fig. 16 indicate that three organic cations generate a dramatic improvement in the **O** state yield (monovalent species **Me_4N** and **Et_4N**, and divalent species **C_3Me_6**; see Fig. 15 for the structures). In particular **Et_4N** produces a 5.4-fold increase in **O** state yield, which translates to a potential improvement of **P** & **Q** formation from 3% to 16%. Our simulations indicate that optimal performance is obtained at approximately 10% conversion, so other organic cations will also be investigated to find the best compromise involving yield, stability and synthetic convenience.

The key advantage of using this chemical approach, as opposed to genetic engineering, is that the extent of the **O** state population and lifetime enhancement can be tailored accurately to achieve a specific goal. This observation follows from the fact that there is a very large number of possible organic cations, and by varying either structure and/or molecular weight, systematic control can be achieved.

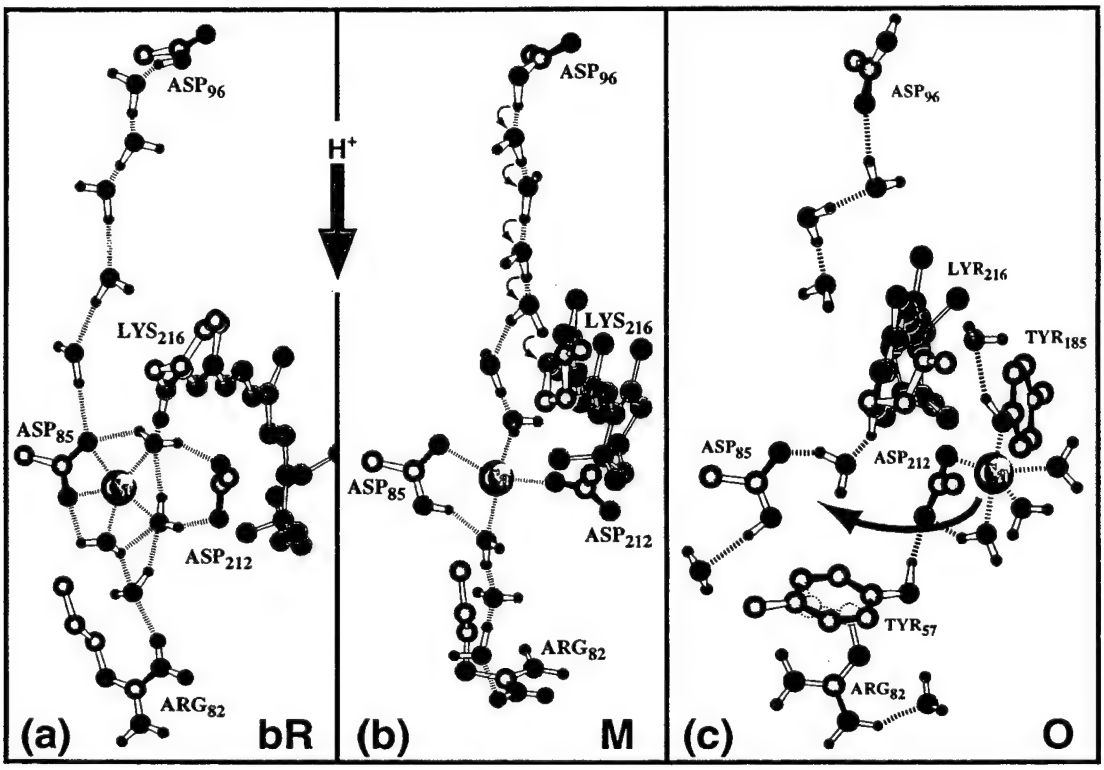

Figure 17. Molecular models of the **bR**, **M** and **O** states of bacteriorhodopsin showing the chromophore, selected amino acid residues and the near-chromophore calcium binding site. Direction towards the cytoplasmic and extracellular surfaces and the proton pumping vector are indicated. Microwave absorptivity experiments suggest that in native **bR**, the calcium enters the proton channel and provides an electrostatic gate preventing back transfer of the proton during the latter stages of the photocycle [37]. The arrow in the **O** state diagram indicates the migration of the cation back to its native position during the **O** → **bR** reaction.

We close this section with an hypothesis on how the organic cations are affecting the yield of the **O** state. Molecular modeling suggests that the **O** → **bR** reaction requires a migration of the cation (calcium in the native protein) as shown in Fig. 17. Thus, as the molecular weight of the cation increases, the decay of the **O** state is slowed. Thus, an increase in molecular weight of the cation will increase the yield of the **O** state for kinetic reasons. However, at some point the cation becomes too large to occupy the native cation binding site, and thus an alternative site is found that is less restrictive. We believe this site is closer to the cation binding site shown for **bR** (see discussion of the two models of the **O** state cation binding sites in Ref. [37]). Thus, there is a maximum in the yield versus molecular weight graph (Fig. 15b).

6. Comments and Conclusions

The prototype shown in Fig. 4 was redesigned to permit the use of commercially available laser diodes and CCD array detectors. The goal was to make a small-scale level II prototype to explore more fully the commercial viability of our architecture, examine better methods of paging and test new protein analogs developed in the latter stages of this contract. The key observation was a factor of four improvement in the reliability of the read operation as discussed in Section 5E. We have not as yet found a spatial light modulator that has sufficient reliability and dynamic range to function adequately in our design. We have not had the financial resources to purchase and try the ferroelectric modulators that are currently being developed at the Univ. of Colorado. We hope to do so in the future.

The protein bacteriorhodopsin has many characteristics that are near-optimal for use in the branched-photocycle architecture. However, it is unrealistic to expect that nature has optimized the protein for this particular application, and we will continue our investigation of chemically and genetically modified bacteriorhodopsin proteins to identify candidates that improve performance. While the organic cation analog proteins show great promise, we have not fully evaluated the potential of site-directed mutagenesis to enhance the branching photochemistry. Through a collaboration with Prof. Richard Needleman, we are initiating a study of selected mutants with extended **O** state lifetimes and yields to determine the impact of these mutations on the performance of the protein in the branched-photocycle architecture. Recent studies indicate that the **O** state lifetime and population can be increased significantly by using Glu-204 and Leu-93 mutants [30-32]. When combined with careful pH control [38] and the use of organic cations (see above), we anticipate that we can enhance the amount of **P** and **Q** that are formed by an order of magnitude. This will improve reliability and data write speeds.

Finally, the homogeneity of the memory medium requires improvement. While polyacrylamide provides excellent protein stability, the small cavities that are created following polymerization provide scattering centers that limit resolution and the quality of the read signal image. DuPont Corporation has offered to help us identify new polymers that will provide adequate stabilization of the protein while improving homogeneity of the data cuvettes. Hybrid polymers involving various combinations of polyvinyl alcohol and gelatin will be investigated. We are working with DuPont scientists currently. We have also established a collaboration with one of Canada's leading young polymer chemists, Prof. Wayne Wang at Carleton University (Ottawa). He has already demonstrated that a co-polymer decreases scattering. We are in the process of setting up a formal collaboration with Prof. Wang to explore the use of co-polymers in stabilizing the protein in 3D memory cuvettes.

7. References.

1. M.A. El-Sayed, On the molecular mechanisms of the solar to electric energy conversion by the other photosynthetic system in nature, bacteriorhodopsin, *Accts. Chem. Res.* **25**, 279-286 (1992).

2. J.K. Lanyi, Bacteriorhodopsin as a model for proton pumps, *Nature* **375**, 461-463 (1995).

3. R.A. Mathies, S.W. Lin, J.B. Ames and W.T. Pollard, From femtoseconds to biology: Mechanism of bacteriorhdopsin's light-driven proton pump, *Annu. Rev. Biophys. Biophys. Chem.* **20**, 491-518 (1991).

4. K.J. Rothschild, FTIR difference spectroscopy of bacteriorhodopsin: toward a molecular model, *J. Bioenerg. Biomembr.* **24**, 147-167 (1992).

5. R.R. Birge, Photophysics and molecular electronic applications of the rhodopsins, *Annu. Rev. Phys. Chem.* **41**, 683-733 (1990).

6. R.A. Mathies, C.H. Brito Cruz, W.T. Pollard and C.V. Shank, Direct observation of the femtosecond excited-state cis-trans isomerization in bacteriorhodopsin, *Science* **240**, 777 (1988).

7. Y. Shen, C.R. Safinya, K.S. Liang, A.F. Ruppert and K.J. Rothschild, Stabilization of the membrane protein bacteriorhodopsin to 140°C in two-dimensional films, *Nature* **366**, 48-50 (1993).

8. D. Oesterhelt, C. Bräuchle and N. Hampp, Bacteriorhodopsin: a biological material for information processing, *Quart. Rev. Biophys.* **24**, 425-478 (1991).

9. R.R. Birge, Protein based optical computing and optical memories, *IEEE Computer* **25**, 56-67 (1992).

10. R.R. Birge, Three-dimensional optical memories, *Amer. Sci.* **82**, 349-355 (1994).

11. R.R. Birge, Protein-based computers, *Scientific American* **272**, 90-95 (1995).

12. A. Popp, M. Wolperdinger, N. Hampp, C. Bräuchle and D. Oesterhelt, Photochemical conversion of the O-intermediate to 9-cis-retinal-containing products in bacteriorhodopsin films, *Biophys. J.* **65**, 1449-1459 (1993).

13. D.A. Parthenopoulos and P.M. Rentzepis, Three-dimensional optical storage memory, *Science* **245**, 843-845 (1989).

14. M.E. Marhic, Storage limit of two-photon-based three-dimensional memories with parallel access, *Optics Lett.* **16**, 1272-1273 (1991).

15. A.S. Dvornikov and P.M. Rentzepis, Two photon three-dimensional optical storage memory, *Adv. Chem.* **240**, 161-178 (1994).

16. S. Hunter, F. Kiamilev, S. Esener, D.A. Parthenopoulos and P.M. Rentzepis, Potential of two-photon based 3-D optical memories for high performance computing, *Appl. Opt.* **29**, 2058-2066 (1990).

17. J.F. Heanue, M.C. Bashaw and L. Hesselink, Volume holographic storage and retrieval of digital data, *Science* **265**, 749-752 (1994).

18. K. Curtis and D. Psaltis, Recording of multiple holograms in photopolymer films, *Appl. Opt.* **31**, 7425-7428 (1992).

19. E.G. Paek and D. Psaltis, Optical associative memory using Fourier transform holograms, *Opt. Eng.* **26**, 428-433 (1987).

20. Z. Chen, D. Govender, R. Gross and R. Birge, Advances in protein-based three-dimensional optical memories, *BioSystems* **35**, 145-151 (1995).

21. R.R. Birge and C.F. Zhang, Two-photon spectroscopy of light adapted bacteriorhodopsin, *J. Chem. Phys.* **92**, 7178-7195 (1990).

22. J.A. Stuart, B.W. Vought, C.F. Zhang and R.R. Birge, The active site of bacteriorhodopsin. Two-photon spectroscopic evidence for a positively charged chromophore binding site mediated by calcium, *Biospectroscopy* **1**, 9-28 (1995).

23. R.R. Birge, R.B. Gross, M.B. Masthay, J.A. Stuart, J.R. Tallent and C.F. Zhang, Nonlinear optical properties of bacteriorhodopsin and protein based two-photon three-dimensional memories, *Mol. Cryst. Liq. Cryst. Sci. Technol. Sec. B. Nonlinear Optics* **3**, 133-147 (1992).

24. A.F. Lawrence and R.R. Birge, The potential application of optical phased arrays in two-photon three-dimensional optical memories, *Proc. SPIE* **1773**, 401-412 (1992).

25. R.R. Birge and D.S.K. Govender, *Three-dimensional optical memory*, Syracuse University, U.S., (1993), pp. 1 - .

26. B.M. Becher and J.Y. Cassim, Improved isolation procedures for the purple membrane of Halobacterium halobium, *Prep. Biochem.* **5**, 161-178 (1975).

27. D. Hames, One-dimensional polyacrylamide gel electrophoresis, in *Gel electrophoresis of proteins: a practical approach* vol. IRL Press, Oxford, (1990) pp. .

28. G. Varo and J.K. Lanyi, Thermodynamics and energy coupling in the bacteriorhdopsin photocycle, *Biochem.* **30**, 5016-5022 (1991).

29. G. Varo and J.K. Lanyi, Effects of the crystalline structure of purple membrane on the kinetics and energetics of the bacteriorhodopsin photocycle, *Biochem.* **30**, 7165-7171 (1991).

30. S. Misra, R. Govindjee, T.G. Ebrey, N. Chen, J.-X. Ma and R.K. Crouch, Proton uptake and release are rate-limiting steps in the photocycle of the bacteriorhodopsin mutant E204Q, *Biochemistry* **36**, 4875-4883 (1997).

31. H. Kandori, Y. Yamazaki, M. Hatanaka, R. Needleman, L.S. Brown, H.-T. Richter, J.K. Lanyi and A. Maeda, Time-resolved Fourier transform infrared study of structural changes in the last steps of the photocycles of Glu-204 and Leu-93 mutants of bacteriorhodopsin, *Biochemistry* **36**, 5134-5141 (1997).

32. Y. Gat, N. Friedman, M. Sheves and M. Ottolenghi, Interaction between Asp-85 and the proton-releasing group in bacteriorhodopsin. A study of an O-like photocycle intermediate, *Biochemistry* **36**, 4135-4148 (1997).

33. Y.N. Zhang, M.A. El-Sayed, M.L. Bonet, J.K. Lanyi, M. Chang, B. Ni and R. Needleman, Effects of genetic replacements of charged and H-bonding residues in the retinal pocket on Ca^{2+} binding to deionized bacteriorhodopsin, *Proc. Natl. Acad. Sci. USA* **90**, 1445-1449 (1993).

34. Y.N. Zhang, L.L. Sweetman, E.S. Awad and M.A. El-Sayed, Nature of the individual Ca^{2+} binding sites in Ca^{2+}-regenerated bacteriorhodopsin, *Biophys. J.* **61**, 1201-1206 (1992).

35. E.H.L. Tan, D.S.K. Govender and R.R. Birge, Large organic cations can replace Mg^{2+} and Ca^{2+} ions in bacteriorhodopsin and maintain proton pumping ability, *J. Am. Chem. Soc.* **118**, 2752-2753 (1996).

36. F.M. Menger and S. Wrenn, Interfacial and Micellar properties of Bolaform Electrolytes, *J. Phys. Chem.* **78**, 1387-1390 (1974).

37. R.R. Birge, D.S.K. Govender, K.C. Izgi and E.H.L. Tan, Role of calcium in the proton pump of bacteriorhodopsin. Microwave evidence for a cation-gated mechanism, *J. Phys. Chem.* **100**, 9990-10004 (1996).

38. G. Váró and J.K. Lanyi, Protonation and deprotonation of the M, N, and O intermediates during the bacteriorhodopsin photocycle, *Biochem.* **29**, 6858-6865 (1990).

8. Publications Sponsored in Part by This Contract [publications in 1995 were also sponsored by Rome Contract (F30602-93-C-0059)]:

1. Birge, R. R. 1995. Protein-based computers. *Scientific American* 272: 90-95.

2. Birge, R. R. and R. B. Gross. 1995. Biomolecular optoelectronics. *In* Introduction to Molecular Electronics. M. C. Petty, M. R. Bryce and D. Bloor, eds. Edward Arnold, London, 315-344.

3. Song, Q. W., C. Zhang, C. Y. Ku, M. C. Huang, R. B. Gross and R. R. Birge. 1995. Determination of the thermal expansion and thermo-optical coefficients of a bacteriorhodopsin film. *Optics Commun.* 115: 471-474.

4. Stuart, J. A., B. W. Vought, C. F. Zhang and R. R. Birge. 1995. The active site of bacteriorhodopsin. Two-photon spectroscopic evidence for a positively charged chromophore binding site mediated by calcium. *Biospectroscopy* 1: 9-28.

5. Song, Q. W., C. Y. Ku, R. B. Gross, R. R. Birge, and R. Michalak. 1995. Modified critical angle method for measuring the refractive index of bio-optical materials and its application to bacteriorhodopsin. *J. Opt. Soc. Amer. B.* 12:797-803.

6. Chen, Z., D. Govender, R. Gross, and R. Birge. 1995. Advances in protein-based three-dimensional optical memories. *BioSystems.* 35:145-151.

7. Birge, R. R., Z. Chen, D. Govender, R. B. Gross, S. B. Hom, K. C. Izgi, J. A. Stuart, and B. W. Vought. 1995. Biomolecular photonics based on bacteriorhodopsin. *CRC Handbook of Organic Photochemistry Photobiolology*:1568-1587.

8. Gross, R. B., A. T. Todorov, and R. R. Birge. 1995. The wavelength-dependent refractive index change associated with the blue to pink membrane photochemical conversion in bacteriorhodopsin. *In* Applications of Photonic Technology. Plenum Press, New York. 115-121.

9. Zhang, Y. H., Q. W. Song, C. Tseronis, and R. R. Birge. 1995. Real-time holographic imaging with a bacteriorhodopsin film. *Optics Letters.* 20:2429-2431.

10. Birge, R. R., R. B. Gross, and A. F. Lawrence. 1996. Biomolecular electronics and optical computing. *In* Molecular Electronics. Marcel Dekker, New York. 333-357.

11. Tan, E. H. L., D. S. K. Govender, and R. R. Birge. 1996. Large organic cations can replace Mg^{2+} and Ca^{2+} ions in bacteriorhodopsin and maintain proton pumping ability. *J. Am. Chem. Soc.* 118:2752-2753.

12. Stuart, J. A., J. R. Tallent, E. H. L. Tan, and R. R. Birge. 1996. Protein-based volumetric memory. *Proc. IEEE Nonvol. Mem. Tech. (INVMTC).* 6:45-51.

13. Gu, L. Q., C. P. Zhang, A. F. Niu, J. Li, G. Y. Zhang, Y. M. Wang, M. R. Tong, J. L. Pan, Q. W. Song, B. Parsons, and R. R. Birge. 1996. Bacteriorhodopsin based photonic logic gate and its application to gray level image subtraction. Optics Commun. 131:25-30.

14. Tallent, J., Q. W. Song, Z. Li, J. Stuart, and R. R. Birge. 1996. Effective photochromic nonlinearity of dried blue-membrane bacteriorhodopsin films. *Optics Letters.* 21:1339-1341.

15. Birge, R. R., B. A. Parsons, Q. W. Song, and J. R. Tallent. 1997. Protein based optical processors and memories. *In* Molecular Electronics. M. Ratner and J. Jortner, Eds., Blackwell Science, London. pp. 439-471.

9. Patents

Patents P2 and P3 were based on previous Rome Laboratory contracts, with patent P3 based on the most recent prior contract (F30602-93-C-0059). Patent P4 was sponsored by the National Institutes of Health, but directly impacts the research reported here, because it described the preparation of organic cation protein analogs.

P1. Optical random access memory. R.R. Birge and A.F. Lawrence, U.S. Patent Number 5,228,001; July 13, 1993.

P2. Three-Dimensional Optical Memory. R.R. Birge and D.S.K. Govender, U.S. Patent Number 5,253,198; October 12, 1993.

P3. Branched-Photocycle Optical Memory. R.R. Birge, U.S. Patent Number 5,559,732; September 24, 1996.

P4. Analog Bacteriorhodopsin Molecules. E. H. L. Tan and R. R. Birge, U.S. Patent Applied For (Application Date October 15, 1996).

MISSION OF ROME LABORATORY

Mission. The mission of Rome Laboratory is to advance the science and technologies of command, control, communications and intelligence and to transition them into systems to meet customer needs. To achieve this, Rome Lab:

a. Conducts vigorous research, development and test programs in all applicable technologies;

b. Transitions technology to current and future systems to improve operational capability, readiness, and supportability;

c. Provides a full range of technical support to Air Force Material Command product centers and other Air Force organizations;

d. Promotes transfer of technology to the private sector;

e. Maintains leading edge technological expertise in the areas of surveillance, communications, command and control, intelligence, reliability science, electro-magnetic technology, photonics, signal processing, and computational science.

The thrust areas of technical competence include: Surveillance, Communications, Command and Control, Intelligence, Signal Processing, Computer Science and Technology, Electromagnetic Technology, Photonics and Reliability Sciences.